Cannabinoid type 2 receptors mediate a cell type-specific plasticity in the hippocampus

Stempel, A.V., Stumpf, A., Zhang, H.Y., Oezdogan, T., Pannasch, U., Theis, A.K., Otte, D.M., Wojtalla, A., Racz, I., Ponomarenko, A., Xi, Z.X., Zimmer, A., Schmitz, D.

Neuron
2016 MAY 18 ; 90(4): 795-809
doi: 10.1016/j.neuron.2016.03.034
Publisher: Cell Press / Elsevier

Cannabinoid Type 2 Receptors Mediate a Cell Type-Specific Plasticity in the Hippocampus

A. Vanessa Stempel[1,9,*], Alexander Stumpf[1], Hai-Ying Zhang[2], Tuğba Özdoğan[1], Ulrike Pannasch[1], Anne-Kathrin Theis[1], David-Marian Otte[3], Alexandra Wojtalla[3], Ildikó Rácz[3], Alexey Ponomarenko[4,5], Zheng-Xiong Xi[2], Andreas Zimmer[3], Dietmar Schmitz[1,4,6-8,*]

[1]Neuroscience Research Center NWFZ, Berlin, Germany
[2]Intramural Research Program, National Institute on Drug Abuse, Baltimore, MD, USA
[3]Institute of Molecular Psychiatry, University of Bonn, Bonn, Germany
[4]NeuroCure Cluster of Excellence, Berlin, Germany
[5]Leibniz-Institut für Molekulare Pharmakologie (FMP), Berlin, Germany
[6]Bernstein Center for Computational Neuroscience (BCCN), Berlin, Germany
[7]Center for Neurodegenerative Diseases (DZNE), Berlin, Germany
[8]Einstein Center for Neurosciences, Berlin, Germany
[9]Present address: MRC Laboratory of Molecular Biology, Cambridge, UK

*Correspondence: vstempel@mrc-lmb.cam.ac.uk (A.V.S.), dietmar.schmitz@charite.de (D.S.)
http://dx.doi.org/10.1016/j.neuron.2016.03.034

SUMMARY

Endocannabinoids (eCBs) exert major control over neuronal activity by activating cannabinoid receptors (CBRs). The functionality of the eCB system is primarily ascribed to the well-documented retrograde activation of presynaptic CB_1Rs. We find that action potential-driven eCB release leads to a long-lasting membrane potential hyperpolarization in hippocampal principal cells that is independent of CB_1Rs. The hyperpolarization, which is specific to CA3 and CA2 pyramidal cells (PCs), depends on the activation of neuronal CB_2Rs as shown by a combined pharmacogenetic and immunohistochemical approach. Upon activation, they modulate the activity of the sodium-bicarbonate co- transporter, leading to a hyperpolarization of the neuron. CB_2R activation occurred in a purely self-regulatory manner, robustly altered the input/output function of CA3 PCs and modulated gamma oscillations in vivo. To conclude, we describe a cell type-specific plasticity mechanism in the hippocampus that provides evidence for the neuronal expression of CB_2Rs and emphasizes their importance in basic neuronal transmission.

INTRODUCTION

The eCB system is one of the main neuromodulatory systems acting in the CNS and is highly conserved across species (Liu et al., 2009). It predominantly functions by modulating neural excitability through presynaptic inhibition of transmitter release and eCB-dependent forms of short- and long-term plasticity (Brenowitz and Regehr, 2005; Carta et al., 2014; Chevaleyre and Castillo, 2004; Hájos et al., 2002; Kim and Alger, 2010; Marsicano et al., 2003; Monory et al., 2006; Stella et al., 1997). Endocannabinoid-mediated plasticity mechanisms are found at both excitatory and inhibitory synapses in most brain areas (Kano et al., 2009) and they primarily depend on a Ca^{2+}-dependent postsynaptic release of eCBs and the retrograde activation of presynaptically located CB_1Rs, which are abundantly expressed in most cell types (Katona and Freund, 2012; Katona et al., 1999). The retrograde mode of action has first been described for two prominent forms of eCB-mediated short-term synaptic depression: depolarization-induced suppression of inhibition (DSI) and excitation (DSE, for reviews see (Castillo et al., 2012; Wilson and Nicoll, 2002)). Yet, depending on the mode of activation, they mediate long-term forms of eCB-mediated plasticity of transmitter release as well (Chevaleyre and Castillo, 2003; Gerdeman et al., 2002; Robbe et al., 2002).

In stark contrast to the vast amount of literature on CB_1R-mediated phenomena, very little is known about the relevance of CB_2Rs in neuronal signaling. Indeed, until recently the CB_2R was referred to as the 'peripheral' CBR reflecting its predominant expression in organs of the immune system (Munro et al., 1993) where it participates in the regulation of immune responses and is responsible for the anti-inflammatory effects of cannabis (Buckley et al., 2000). A major problem of studying CB_2Rs has been their low expression levels in the CNS and the lack of reliable antibodies, which has sparked controversy concerning their localization in the brain (Baek et al., 2013; Marchalant et al., 2014). Yet, the generation of CBR knockout (KO) mice (Buckley et al., 2000; Zimmer et al., 1999) and the production of a diverse array of synthetic cannabinoid agents have advanced and facilitated research on CB_2Rs. Especially behavioral studies have advocated the presence of CB_2Rs in the CNS (Onaivi, 2006; Van Sickle et al., 2005) with properties that extend their neuro-immunological function. Anatomical and electrophysiological studies support this notion and suggest a role of CB_2Rs in neural transmission and excitability (den Boon et al., 2012; Gong et al., 2006; Morgan et al., 2009). In the hippocampus, the presence of CB_2Rs has been suggested (Brusco et al., 2008; Kim and Li, 2015; Li and Kim, 2015) but their physiological role is uncertain. Furthermore, it is not clear whether they are expressed neuronally or mainly in cells of the immune system, such as microglia (Schmöle et al., 2015).

In this paper, we provide *in vitro* and *in vivo* evidence that functional CB_2R are expressed neuronally in the hippocampus and that they mediate a self-regulatory eCB-mediated plasticity in a distinct subset of hippocampal principal cells via modulation of the sodium/bicarbonate co-transporter (NBC).

RESULTS

Backpropagating Action Potentials Induce a Cell Type-Specific Hyperpolarization in Hippocampal Principal Cells

In response to trains of action potentials (APs) we observed a long-lasting membrane potential (V_m) hyperpolarization in CA3 pyramidal cells (PCs), which outlasts the classic afterhyperpolarization (AHP). The hyperpolarization persisted for the duration of the recording (up to 20min after the induction), was as large as ~10mV (Figure 1A), and was present in all cells tested when recorded in perforated patch (pp) configuration, in which the intracellular milieu of the recorded cell remains undisturbed. When repeating the above experiment in whole-cell (wc) configuration, we observed a fraction of unresponsive cells, which might explain why this form of plasticity has not been observed before and thus a cut-off was introduced to classify cells as 'reactive' and 'unreactive' (Figures S1A-B, and see methods). We compared different recording parameters and found a significant correlation between the access resistance (R_a) and the degree of hyperpolarization (Figures S1C-F). We furthermore performed a subset of wc recordings with a potassium gluconate-based internal solution (instead of methanesulfonate), or with 1mg/ml biocytin, in both of which we observed a complete abolition of the hyperpolarization (data not shown). Although the reasons for this are unresolved, many studies have previously reported that internal solutions and anions alter and interfere with membrane properties (Eckert et al., 2001; Kaczorowski et al., 2007).

To elucidate whether this hyperpolarization is a mechanism common to all hippocampal principal cell types or displays cell-type specificity, we examined CA1 PCs and dentate gyrus granule cells (DG GCs, both recorded in pp configuration), as well as CA2 PCs. In contrast to CA3 PCs that hyperpolarized to similar extents independent of their location within CA3, neither CA1 PCs nor DG GCs hyperpolarized in response to AP trains (Figures 1B-C). This induction failure could be the result of a different induction threshold. To test for this, we used a theta-frequency burst protocol, consisting of four times as many APs as the standard protocol (see methods), that is known to trigger eCB-mediated long-term depression (LTD) in these cells

(Younts et al., 2013). However, this also failed to induce a long-lasting hyperpolarization in CA1 PCs (Figures S2A-C). Contrary to this, morphologically identified CA2 PCs do express this form of cellular plasticity (Figures S2D-F).

The Long-Lasting Hyperpolarization Is Dependent on the Release of Endogenous 2-AG and Neuronal Cannabinoid Type 2 Receptors

What could be the underlying mechanism of this self-inhibitory long-term plasticity? eCBs are known to modulate many forms of long-term plasticity in the CNS (Chevaleyre et al., 2006) and high frequency stimulation (HFS) has been shown to lead to release of 2-arachidonoylglycerol (2-AG) in hippocampal slices (Stella et al., 1997). To assess whether the activity-dependent release of 2-AG – the most ubiquitous eCB in the CNS that is synthesized and released upon a sufficient rise in intracellular calcium (Sugiura et al., 2002) – mediates the plasticity, we recorded from mice lacking the 2-AG-synthesizing enzyme DAGLα (Jenniches et al., 2015). To confirm the lack of 2-AG synthesis in the DAGLα KOs, we recorded DSI in DAGL$\alpha^{-/-}$ CA3 PCs since 2-AG is the main eCB involved in both DSI and DSE (Hashimotodani et al., 2008). In contrast to WT controls, DSI was completely abolished in DAGL$\alpha^{-/-}$ CA3 PCs as measured by the change in amplitude and frequency of spontaneous inhibitory postsynaptic currents (sIPCSs, Figures 2A-B). Next, we tested whether lack of 2-AG would have an effect on the AP-mediated hyperpolarization and found that it was also absent in these animals (Figures 2C-D), thereby establishing that this effect is dependent on AP-driven 2-AG release.

The main CBRs that eCBs act on are CB_1 and CB_2. Previously, it has been reported that CB_1Rs activate G protein-coupled inwardly-rectifying potassium channels (GIRK) on subsets of cortical neurons in response to AP trains (Bacci et al., 2004; Marinelli et al., 2009). This phenomenon, termed slow self-inhibition (SSI), also leads to a long-lasting V_m hyperpolarization. To test whether the same mechanism may underlie the hyperpolarization, we recorded CA3 PCs from $CB_1R^{-/-}$ mice, but found that the effect was fully intact in these animals (Figure 3A). We then recorded CA3 PCs from $CB_2R^{-/-}$ mice – the other main CBR. Surprisingly, the effect was absent in these animals, suggesting that CB_2Rs mediate the long-lasting hyperpolarization (Figure 3B).

Assuming that CB_2Rs mediate the AP-induced hyperpolarization, preincubation of slices with CBR antagonists should abolish the effect in WT and as well as CB_1R KO animals. Firstly, we confirmed that the percentage of reactive cells recorded in wc configuration was comparable between $CB_1R^{-/-}$ and WT CA3 PCs, and that the hyperpolarization was absent in CB_2R KOs (Figures S3A-B). We then preincubated slices with the mixed cannabinoid inverse agonist AM-

251 that, as predicted, blocked the AP-induced hyperpolarization in both WT and CB_1R-mutant CA3 PCs (Figures S3C-D). It is of note that this result indicates that AM-251 efficiently targets CB_2Rs at concentrations that are commonly considered to be CB_1R-specific (2-5μM). In addition, we preincubated slices from $CB_1R^{-/-}$ mice with the CB_2R-specific inverse agonist SR144528 (SR) that successfully blocked the hyperpolarization in all cells tested (Figures S3C-D). These results support the presence of functional CB_2Rs that can be blocked pharmacologically.

It is known that CB_2Rs are expressed in macrophage lineage cells including microglia that have been shown to modulate neuronal transmission (Salter and Beggs, 2014). Furthermore, as of yet, direct evidence for the neuronal expression of CB_2Rs is still negligible, due to the lack of specific antibodies and neuron-specific genetic manipulations. Thus, to verify this unexpected finding and in order to test for the neuronal expression of CB_2Rs we generated a neuron-specific CB_2R KO mouse in which the CB_2R-encoding gene *Cnr2* is deleted under a synapsin promoter via the Cre/loxP system (Syn-CB_2R KO, see methods and Figure S4). We find that in these mice the hyperpolarization was equally absent as in the constitutive KO (Figure 3C). Importantly, the hyperpolarization in the $CB_2R^{+/+}$ littermate controls was not different from C57BL/6 WT (Mann-Whitney test: P=0.67, Figure 3D). As a general control for the properties of CA3 PCs recorded from the mutant mice used, we compared their basic intrinsic physiological properties, which were not different from C57BL/6 or littermate WT mice (Figure S3E). Thus any changes observed are unlikely to stem from differences in their basal properties. In summary, these results strongly suggest that the hyperpolarization depends on the activation of neuronal CB_2Rs and is independent of CB_1R activation (Figures 3E-F).

To support this finding, we performed *in situ* hybridization assays (ISH) for CB_2R mRNA in hippocampi of Syn-CB_2R KO (Figures 4A-C and S4) and CB_2R KO (Figure S6) mice. Figure 4 shows the RNAscope ISH results, illustrating co-localization of *Cnr2* (green) and *Rbfox3* (a neuronal marker gene that encodes NeuN, red) in the majority of hippocampal neurons in the CA3 region in WT, but not in Syn-CB_2R KO mice (Figures 4A-C). We detected similar amounts of CB_2R mRNA in area CA2, but much lower levels in areas CA1 and DG (Figure S5).

We noted that *Cnr2* was still detectable in hippocampal tissue of Syn-CB_2R KO mice (Figure 4C, lower panels), which may reflect *Cnr2* expression in glial cells. To test this hypothesis, we used fluorescence-activated cell sorting (FACS) to separate hippocampal neuronal cells and glial cells (Fig. 4D), and then used quantitative PCR (qPCR) to measure *Cnr2* expression levels in each cell population. We find that *Cnr2* is mainly expressed in NeuN+ cells (neurons) in WT, while it was substantially reduced (~70% reduction) in Syn-CB_2R KO and completely abolished

in CB_2R KO mice (Fig. 4E). As expected, we detected CB_2R mRNA also in non-neuronal cells in WT and Syn-CB_2R KO, but not in CB_2R KO mice (Figure 4E). Unexpectedly, low levels of *Cnr2* gene are still detectable in NeuN+ cells in Syn-CB_2R KO mice (Fig. 4E), which may be related to the impurity of the sorted neurons; e.g. a small fraction of glial cells may 'contaminate' the NeuN+ population. To test this hypothesis, we examined *Rbfox3* and the glial marker genes *Itgam*, *Cspg4* and *Aldh1L1*, which encode CD11b (a microglial marker), NG-2 (an oligodendrocyte marker) and ALDH1L1 (an astrocyte marker) respectively, in each cell population. We detect a small percentage (~25%) of glial markers in the NeuN+ population (Figure 4G-a). Since glial cells also express *Cnr2* (Figure 4E), this may well explain why low levels of *Cnr2* expression (~30%) are detectable in NeuN+ cells of Syn-CB_2R KO mice. As a control, we analyzed the same samples for CB_1R mRNA expression, which was not different between NeuN+ (and NeuN-) cells of WT, Syn-CB_2R KO and CB_2R KO mice (Figure 4F). To further confirm this finding, we compared *Cnr2* expression between WT, CB_1R and CB_2R KO mice with classical ISH in combination with immunostainings. We find a similar degree of co-localization of *Cnr2* with NeuN and vGluT2 (a marker for glutamatergic neurons) in WT and CB_1R KO mice, while *Cnr2* is undetectable in the CB_2R KO (Fig. S5).

The activity-induced hyperpolarization can be mimicked and occluded by CBR agonists

As a further line of evidence supporting the presence of functional CB_2Rs, we tested whether we can mimic the AP-driven hyperpolarization by directly activating CB_2Rs pharmacologically. The mixed CBR agonists 2-AG and WIN,55212-2 (WIN), as well as the CB_2R-specific agonist HU-308 (HU), all strongly hyperpolarized CA3 PCs in WT mice (Figures 5A-C,E-F). To confirm that the drug-induced hyperpolarization is indeed due to CB_2R activation and as a control for the specificity of HU for CB_2Rs at the concentration used, we tested 2-AG and HU in slices of and (Syn-)$CB_2R^{-/-}$ mice. Neither of the drugs led to a hyperpolarization in these animals, strongly arguing for a purely CB_2R-dependent mechanism (Figures 5D-F). Additionally, late application of AM-251 could reverse the hyperpolarization induced by 2-AG, arguing for the same target receptor (Figure 5G). To substantiate the assumption of a shared CB_2R-dependent mechanism between AP-dependent release of endogenous 2-AG and exogenously applied CBR agonists, we performed occlusion experiments. When the agonist HU was applied before AP trains, and also when these stimuli were applied in the reverse sequence, the maximal CB_2R activation via one process occluded the other, as the respective second stimulus failed to elicit an additional hyperpolarization (Figures 5H-I).

The hyperpolarization is mediated by a G Protein- and sodium-dependent modulation of the NBC

As CBRs are G Protein-coupled receptors (GPCRs), we confirmed that the hyperpolarization is mediated by a G Protein-dependent cascade by performing experiments with 0.5mM GDPßS, a non-hydrolysable GDP analog that blocks G protein-coupled activity. The inclusion of GDPßS into the pipette abolished the pharmacologically-induced hyperpolarization within the manipulated neuron (Figures 6A-B), supporting the idea of a cell-intrinsic, G Protein-dependent mechanism.

CBRs, like many other neuronal GPCRs, couple to GIRK channels (Ho et al., 1999; Mackie et al., 1995) which at a first glance appear as a likely downstream target of CB_2R activation to mediate the hyperpolarization via an extrusion of potassium from the cell. However, when analyzing the pharmacologically induced hyperpolarization, we observed no change in input resistance concurrent with the hyperpolarization (Figures 6C-E). As a control for a GPCR-dependent activation of GIRK, we recorded from CA3 PCs and applied 1µM Adenosine that is known to act on adenosine receptors that in turn activate GIRK. As expected for a conductance-based mechanism, we find a significant reduction of the R_{in} that is furthermore reversed by the GIRK antagonist SCH-23390 (Figure S7A). In contrast to this, the acute application of SCH-23390 failed to repolarize the V_m of CA3 PCs after the successful induction of the hyperpolarization by both AP- dependent release of 2-AG and pharmacological CB_2R activation (Figure S7B). We also analyzed the current-voltage relationship with step protocols before and after CB_2R activation (Figure 6E). To conclude, in contrast to cortical SSI, which is mediated by GIRK channels, this set of experiments strongly argues against a conductance-based process and the involvement of GIRK channels in the hyperpolarization.

Next, we thus investigated the involvement of ionic gradients and electrogenic pumps. In a first set of experiments we blocked the sodium/chloride co-transporter KCC2 (with 10µM VU0240551), the sodium/potassium/chloride co-transporter NKCC (with 10µM Bumetanide) and the sodium/hydrogen exchanger (with 10µM Cariporide), but could not antagonize the long-lasting hyperpolarization. Further, we removed either chloride or potassium from the media, however, the effect was still fully intact (data not shown). Finally, replacing sodium with N-Methyl-D-glucamin (NMDG) resulted in a complete abolishment of the agonist-induced hyperpolarization (Figure 6F). Furthermore, preincubation with a specific blocker of the NBC prevented the long-lasting hyperpolarization, both for agonist as well as AP-driven induction (Figures 6F-J), arguing for the specific involvement of the NBC. To rule out that mere interference with the V_m – via the change of intra- and extracellular sodium concentrations – occludes the hyperpolarization, we preincubated slices with a blocker for the sodium/potassium pump that is expressed in CA3 PCs

and has been shown to hyperpolarize neurons in an activity-dependent manner as well (Gustafsson and Wigström, 1983). Yet, in the presence of 10µM ouabain, the hyperpolarization was fully intact (in contrast to NBC block and NMDG replacement, summary graph: Figures 6I-J). To conclude, we found that the hyperpolarization is dependent on a) extracellular sodium and its gradient across the membrane and b) the activity of the NBC.

Acute reversal of the hyperpolarization by CB_2R inverse agonists

What is the underlying cause of the long-lasting nature of the hyperpolarization? HFS can increase 2-AG levels for several minutes (Stella et al., 1997) and it has been shown that eCB-mediated LTD of inhibitory inputs can be reversed by applying AM-251 5min, but not 10min, after the induction (Chevaleyre and Castillo, 2003). Additionally, it has previously been suggested that antagonists can acutely reverse other forms of long-term plasticity such as mGluR-dependent LTD (Palmer et al., 1998) which is likely to be due to a persistent receptor activation even in an agonist-unbound state (Lodge et al., 2013). To test for these possibilities, we firstly performed control recordings in WT CA3 PCs for >25min to confirm the feasibility of pharmacological manipulation during longer recordings (Figures S8A-B). In a separate set of experiments, we then acutely applied the CB_2R-specific inverse agonist SR after eliciting the hyperpolarization in CA3 PCs with the AP protocol. We found that late application of SR repolarized the V_m back to its baseline levels in all cells tested (Figures S8C-E). Because we applied the drug at different time points (~5-15min after the induction, Figure S8C) and could reverse the hyperpolarization even 15min after induction, it is unlikely to still depend on elevated 2-AG levels. Thus, this data set suggests that constitutive receptor activation may be the mechanism underlying the persistency of this particular form of plasticity. We performed these experiments in $CB_1R^{-/-}$ animals to eliminate possible off-target effects of the pharmacological agent.

Comparison of CB_2R- versus presynaptic eCB-mediated effects

Do CB_2Rs also modulate 'classic' eCB-mediated alterations of presynaptic function and does the hyperpolarization have similar characteristics? First, we tested whether the hyperpolarization depends on synaptic transmission and found that it was intact in block of both excitatory and inhibitory transmission (Figure 7A). Second, DSI has been shown to be a mechanism that acts in an auto- and paracrine manner (Kreitzer et al., 2002; Wilson and Nicoll, 2001 but see Younts et al., 2013). To test if the AP-driven release of 2-AG by one neuron is sufficient to elicit a hyperpolarization in neighboring neurons, we performed dual pp recordings of adjacent CA3 PCs (distance between pipette tips: 11±1.2µm) and found no evidence for a detectable 'spread' of the

effect between PCs (Figure 7C-D). Third, to test whether CB_2R activation could mimic DSI, we recorded evoked IPSCs (eIPSCs) in CA3 PCs and induced DSI by depolarization of the recorded neuron. Conversely, subsequent application of 1µM HU did not alter the eIPSC amplitude of DSI+ neurons (Figure 7E). Additionally, the reduction of field excitatory postsynaptic potentials (fEPSPs, recorded in CA3) observed upon application of the mixed CBR agonist WIN, which is also ascribed a presynaptic mode of action (Takahashi and Castillo, 2006), could not be mimicked by HU (Figure 7F). To conclude, the hyperpolarization appears to be a solely self-regulatory cell-intrinsic mechanism that acts complementary to presynaptic CBRs.

Physiological stimulation and functional significance of CB_2Rs

We assessed the functional significance of CB_2R activation on both a single cell and network level. In stark contrast to the so far employed artificial fixed-frequency induction protocol, both the frequency and amount of neuronal spiking *in vivo* are irregular, highly variable and temporally complex. CA3 PCs in particular are known to spike frequently when recorded *in vivo*, both as single spikes and in bursts (Sneider et al., 2006). We thus considered whether physiologically relevant activity patterns are able to induce the hyperpolarization and constructed a spike train based on *in vivo* place field firing patterns of CA3 PCs (see methods). Indeed, we found that this physiological spike train (PST) elicited a hyperpolarization with an average ΔV_m that did not differ from the standard protocol (unpaired t-test: p=0.42, Figures 8A-C).

Next, we investigated whether the long-lasting hyperpolarization affects the output of CA3 PCs. We therefore compared the spike probability of synaptically evoked AP firing in CA3 PCs before and after the application of HU. In those cells that hyperpolarized (wc: 5/8 reactive cells) we find a simultaneous, robust reduction in spike probability by >80% (Figures 8D-F). To test whether this was causally linked to the hyperpolarization induced by the CB_2R agonist, we "clamped" the cells to their initial baseline V_m with constant current injection at the end of each experiment. As expected, this was sufficient to restore the initial spike probability in all neurons (0.93±0.04, normalized to 1). Conversely, when we manually hyperpolarized the unreactive cells with current injections (baseline V_m: -64.7±0.8mV, hyperpolarized V_m: -72.5±0.5mV), we were able to mimic the reduction in spike probability induced by the CB_2R agonist-mediated hyperpolarization (0.1±0.036, normalized to 1). In summary, these experiments indicate that the V_m hyperpolarization following activation of CB_2Rs significantly shifts the rheobase of CA3 PCs and profoundly reduces their input/output function.

Finally, to study the role of CB_2R signaling in network dynamics we recorded local field potentials (LFP) in area CA3 of freely behaving mice that were systemically treated with the CB_2R

agonist HU, or vehicle. LFP oscillations in the slow gamma band (30-85Hz), generated locally in area CA3 (Csicsvari et al., 2003), and theta (5-10Hz) oscillations determine hippocampal network synchronization and information processing during exploratory behavior. During baseline recordings and after vehicle administration, the amplitude of gamma oscillations changed as a function of the theta phase, more pronounced variations of gamma amplitude were found during theta cycles of higher amplitude (Figure 8G, upper panel), in agreement with earlier reports (Schomburg et al., 2014; Wulff et al., 2009). In contrast, following the agonist administration, slow gamma modulation was significantly less strongly determined by changes of theta oscillation amplitude in WT mice (Figure 8G, lower panel) but not in Syn-$CB_2R^{-/-}$ mice ($F_{1,10}$=0.3, p=0.59). The power of theta and gamma oscillations as well as the theta modulation of intermediate (65-120Hz) gamma oscillations were not affected by the agonist treatment (power: $F_{1,13}$=1.0, p=0.33 and $F_{1,13}$=1.5, p=0.24; modulation: Figure 8H). Additional LFP recordings in area CA3 of behaving Syn-$CB_2R^{-/-}$ mice and their WT littermates revealed a reduced power of gamma oscillations in the mutant (Figure S9). Altogether, these results suggest that neuronal CB_2Rs regulate gamma oscillations in area CA3 *in vivo*.

Discussion

CB_2Rs have been reported to be modulated during a variety of complex neuropsychiatric disorders including depression, schizophrenia and autism spectrum disorders and, due to their non-psychotropic mode of action, are considered promising therapeutic targets (Onaivi, 2011). Yet, in contrast to the well-established function and localization of CB_1Rs, little is known about their role in basic neurotransmission. By providing a first description of functional, neuronally expressed CB_2Rs in area CA3 of the hippocampus, our findings now reveal a novel role for CB_2Rs in the CNS and challenge the classic, CB_1R-focused view on eCB function.

In summary, we find that neuronal CB_2Rs mediate a long-lasting, cell-intrinsic hyperpolarization in hippocampal principal neurons of areas CA3 and CA2. The CB_2R-dependent hyperpolarization can be triggered via the release of endogenous 2 -AG or by direct pharmacological receptor activation. Because it is long-lasting in its nature and is additionally independent of excitatory and inhibitory synaptic transmission, it appears to be an intrinsic plasticity process that negatively modulates the excitability of CA3 PCs.

Cell type-specific expression of the CB_2R-mediated plasticity. The AP-dependent hyperpolarization can only be induced in CA3 and CA2 PCs, which resemble each other in their electrophysiological properties (Wittner and Miles, 2007) but not in the other two main principal

cell populations of the hippocampus, namely CA1 PCs and DG GCs. This may be either due to a lack of CB_2R protein or due to an induction failure. The former is unlikely since we detect low levels of CB_2R mRNA in these cell populations as well. We thus tested the latter hypothesis and found that we can readily induce a hyperpolarization of CA1 PCs by pharmacological activation of CB_2Rs with both HU and WIN (data not shown). In combination with the finding that even strong stimuli, that are known to trigger eCB-mediated LTD at this synapse (Younts et al., 2013), failed to elicit a hyperpolarization, these results supports the notion that functional CB_2Rs are present in CA1 (and DG) but are not activated by physiological activity. Possible explanations for this induction failure are manifold, including differences in the expression levels and distribution of the CB_2R or other components of the ECS, and highlight the fact that the development of specific CB_2R antibodies (Baek et al., 2013; Marchalant et al., 2014) is crucially important to determine their expression on a (sub-) cellular level.

Neuronal expression of functional CB_2Rs in area CA3. The expression of CB_2Rs in the CNS has been subject to much debate (Onaivi, 2006), with many published studies being unable to detect any CB_2R mRNA or ligand binding in brain preparations or only in microglia (Buckley et al., 2000; Galiègue et al., 1995; Schmöle et al., 2015). However, behavioral and electrophysiological studies have suggested the functional presence of CB_2Rs (Onaivi, 2006; Van Sickle et al., 2005; Xi et al., 2011; Zhang et al., 2014). Therefore, the question remains: are CB_2Rs expressed in neurons? To address this question, we generated a novel, neuron-specific CB_2R KO to use in combination with electrophysiological and molecular biology techniques: firstly, the finding that the CB_2R-mediated hyperpolarization is absent in the neuron-specific CB_2R KO argues for the presence of functional neuronal CB_2Rs at a protein level. Secondly, by means of ISH (with a fluorescence double-labelling strategy) and FACS/qPCR assays, we are able to demonstrate the expression of CB_2R mRNA in hippocampal glutamatergic neurons and, more specifically, CA3 PCs. Taken together, this data provides strong and direct evidence for the neuronal expression of functional CB_2Rs in the CNS.

What underlies the long-lasting hyperpolarization mechanistically? Surprisingly, the hyperpolarization was not accompanied by a change in membrane resistance, which rules out the involvement of a conductance-based mechanism (unlike cortical SSI (Bacci et al., 2004)) and suggests the involvement of an ion pump or co-transporter. CBRs have before been shown to modulate the activity of ion co-transporters, such as the sodium/hydrogen exchanger (Bouaboula et al., 1999). Following this lead, we performed experiments with NMDG-based sodium

replacement that hinted towards a sodium-dependent process. Finally, block of the NBC by a specific antagonist abolished both the AP-driven and pharmacologically induced hyperpolarization, suggesting it to be the downstream target of CB_2R activation.

The NBC is a member of the SLC4 solute carrier family and plays an important role in intracellular pH regulation by accumulating intracellular bicarbonate driven by the inwardly directed sodium gradient (for a review see (Ruffin et al., 2014)). Hippocampal PCs express NBCs (Majumdar et al., 2008) and functional studies indicate a role in pH regulation during neuronal activity (Chesler and Kaila, 1992). Our study provides the first evidence for a functional coupling between cannabinoid signaling and the NBC. Future studies will discover the molecular mechanisms involved in this interaction.

A possible cause for the long-lasting hyperpolarization upon CB_2R activation could be identified based on the observation that the acute application of a CB_2R inverse agonist reversed the AP-triggered hyperpolarization. Given that endogenous 2-AG is broken down rapidly (Sugiura et al., 2002) and other studies estimated the prolonged presence of 2-AG after HFS to be ~5min (Chevaleyre and Castillo, 2003), it is unlikely that 2-AG remains available to constitutively activate the receptor up to 15min after induction. Thus, our data suggests that the transient stimulation of CB_2Rs by activity-evoked release of 2-AG may alter their properties, rendering them persistently active in the absence of agonist, similar to observations on mGluRs (Lodge et al., 2013; Young et al., 2013).

Complementary action of CB_1- and CB_2 receptors. As mentioned in the introduction, membrane-derived lipids including eCBs predominantly function through presynaptic inhibition of transmitter release. Only few studies have demonstrated changes in neuronal excitability that depend on cell-intrinsic eCB modulation (Bacci et al., 2004; den Boon et al., 2012). Thus the question arises, how might CB_2R activation contribute to the fine-tuned, highly complex eCB neuromodulatory system that controls a single neuron's physiology and excitability from presynaptic transmitter release to spike output?

Our data suggests that on a cellular level CB_1- and CB_2Rs may provide a non-overlapping functionality with CB_1Rs being expressed mostly presynaptically and CB_2Rs on postsynaptic compartments of hippocampal CA3/2 PCs. A complementary modulation of the auto-associative CA3 network by 1) CB_1Rs that presynaptically modulate chemical transmission and alter synaptic weights of incoming inputs and 2) CB_2Rs that alter the cell's intrinsic properties in response to AP firing provides a powerful mechanism to fine-tune the network's excitability. This seems especially

important in area CA3 and CA2 that are recurrently connected and thus particularly susceptible to hyperexcitability and imbalanced network states (Le Duigou et al., 2014; Sloviter, 1991). In line with this, the hypothesis of CB_2Rs providing a functional 'safety brake' is plausible. Furthermore, given the long-lasting nature of the hyperpolarization, one might speculate that – especially during ongoing activity *in vivo* – CB_2Rs will provide a rather 'tonic' inhibition.

Physiological relevance of CB_2R activation in the hippocampus. The *in vivo* and *in vitro* analysis of CB_2R function shows that they impact the output of a single CA3 PC as well as altering locally generated network oscillations in the behaving animal. We show that physiological spike trains activate CB_2Rs and that their activation reduces the spike probability of CA3 PCs. Our finding, that a change in the V_m strongly affects the input/output transformation of CA3 PCs, supports the idea that intrinsic membrane properties are highly relevant for single cell excitability and information processing (Kowalski et al., 2015; Lee et al., 2012). The hippocampus exhibits several functionally distinct types of gamma oscillations including locally generated, slow oscillations and intermediate/fast oscillations that originate in the entorhinal cortex and entrain the hippocampus (Colgin et al., 2009; Csicsvari et al., 2003; Schomburg et al., 2014). It is thought that the cross-frequency coupling of hippocampal theta and gamma oscillations as observed during exploratory behaviors may serve as coding scheme for working memory, and to provide the basis for simultaneously encoding of information at different time scales. In the CA3 area gamma oscillations arise from interactions between PCs and interneurons, rendering gamma-synchronization sensitive to changes of excitability of these cell types (Buzsáki and Wang, 2012). We find that acute application of a CB_2R agonist selectively affects the theta-dependent modulation of gamma oscillations in WT but not Syn-$CB_2R^{-/-}$ mice and that Syn-$CB_2R^{-/-}$ mice exhibit reduced power of gamma oscillations. In contrast, the effects of eCBs on network oscillations *in vivo* exerted via CB_1Rs are widespread and affect synchronization across frequency bands (Robbe et al., 2006), suggesting a more specific involvement of CB_2R in spatial coding modes supported by gamma oscillations (Bieri et al., 2014). To summarize, the reduced spike probability of CA3 PCs *in vitro* and the selective disruption of slow gamma oscillations by CB_2Rs activation strongly suggest that neuronal CB_2Rs are important modulators of local network rhythms. Recent studies have suggested that a lack of CB_2Rs impairs hippocampal memory function (García-Gutiérrez et al., 2013; Li and Kim, 2016), similar to the effect of CB_1R deficit in adult mice (Bilkei-Gorzo et al., 2005). Further electrophysiological and behavioral analysis of the Syn-CB_2R KO will hopefully help us gain a better understanding of their role in hippocampal information processing on both a single cell and network level.

Conclusion

In comparison to the vast literature on CB_1R function in the CNS, the current state of knowledge concerning CB_2Rs is negligible. It is thus crucial to highlight their importance in basic neuronal transmission. Our results provide a first in depth description of neuronal CB_2R expression and their functional relevance in the hippocampus.

Experimental Procedures

Ethical statement and animal handling. Animal husbandry and experimental procedures were performed in accordance with the guidelines of local authorities (Berlin, Germany), the German Animal Welfare Act and the European Council Directive 86/609/EEC. KO mice were maintained on a C57BL/6 genetic background and generated in the laboratory of A. Zimmer (Buckley et al., 2000; Jenniches et al., 2015; Zimmer et al., 1999). Neuron-specific, conditional CB_2R KO mice were generated by crossing mice expressing Cre recombinase under the Synapsin I promoter with floxed CB_2R animals.

In vitro electrophysiology. Electrophysiological recordings from hippocampal slices were made as described previously (Maier et al., 2011, 2012). The AP trains (inter-stimulus interval: 10ms, inter-train interval: 20s) were induced with 2ms long, somatic current injections. Pharmacological agents were bath applied. Sample sizes are given as the number of experiments (n) and of animals (N). Normally distributed data sets were compared with a two-tailed Student‘s t-test and values are expressed as mean±SEM. Nonparametric tests were used as indicated and data presented as median (with 25^{th} and 75^{th} percentile). Results were considered significant at $p<0.05$. Given V_m values are not corrected for liquid junction potential. In wc recordings, cells were classified as ‘reactive’ or ‘nonreactive’ based on a 2.1mV cut-off.

In vivo electrophysiology. Mice were implanted with arrays of single tungsten wires in area CA3 and the LFP was recorded while the animals explored freely in an open arena. After 1h of baseline recordings, animals were injected with either vehicle (10mg/kg DMSO) or with HU (10mg/kg, dissolved in DMSO) and were recorded in the arena for one more hour. Phase-amplitude coupling of theta and gamma oscillations was computed as described previously (Wulff et al., 2009). The statistical significance of comparisons was determined by a two-way ANOVA.

Molecular Biology. Standard molecular biology techniques as well as classical ISH, RNAscope ISH and FACS assays were performed as described previously (Buckley et al., 2000; Li et al., 2015; Liu et al., 2014; Zhang et al., 2014). For the RNAscope ISH in the Syn-CB_2R KO, the probes Mm-*Cnr2*-O2 and Mm-*Rbfox3*-C2 were designed and provided by Advanced Cell Diagnostics Inc. For FACS, cells were sorted with a PE-labelled (fluorescent) anti-NeuN antibody (1:500; FCMAB317PE, Millipore) and validated the purity of the detected cell populations with qRT-PCR analysis of *Rbfox3* and *Itgam*, *Cspg4* and *Aldh1l1*.

Author contributions

The study was conceived and designed by DS and AVS, who also wrote the paper. AVS performed all in vitro electrophysiological experiments with the help of AS, UP and AKT, and AVS analyzed all experiments. HYZ and ZXX contributed the ISH and FACS data. The in vivo electrophysiology was performed and analyzed by TÖ and AP. AZ, DMO, AW and IR generated and provided all KO animals. AS, HYZ, TÖ, UP and AKT contributed equally to this study.

Acknowledgements

We thank S Rieckmann and A Schönherr for technical assistance, G Buzsáki, K Diba and R Schmidt for sharing their data, C Böhm and FW Johenning for unpublished experiments, and I Vida, I Katona and A Kulik for their help. Also, we thank JR Geiger, U Heinemann and members of the Schmitz lab for helpful discussions, N Maier for critical comments on an early version of the manuscript, and D Evans for proofreading the final version. This work was supported by the NeuroCure and the ImmunoSensation Clusters of Excellence, the BCCN, the DZNE, the Einstein Foundation and the Deutsche Forschungsgemeinschaft (FOR926, SFB665, SFB958, SPP1665 and GRK1123).

References and Notes

Bacci, A., Huguenard, J.R., and Prince, D.A. (2004). Long-lasting self-inhibition of neocortical interneurons mediated by endocannabinoids. Nature *431*, 312–316.

Baek, J.-H., Darlington, C.L., Smith, P.F., and Ashton, J.C. (2013). Antibody testing for brain immunohistochemistry: Brain immunolabeling for the cannabinoid CB2 receptor. J. Neurosci. Methods *216*, 87–95.

Bieri, K.W., Bobbitt, K.N., and Colgin, L.L. (2014). Slow and Fast Gamma Rhythms Coordinate Different Spatial Coding Modes in Hippocampal Place Cells. Neuron *82*, 670–681.

Bilkei-Gorzo, A., Racz, I., Valverde, O., Otto, M., Michel, K., Sastre, M., and Zimmer, A. (2005). Early age-related cognitive impairment in mice lacking cannabinoid CB1 receptors. Proc. Natl. Acad. Sci. U. S. A. *102*, 15670–15675.

den Boon, F.S., Chameau, P., Schaafsma-Zhao, Q., van Aken, W., Bari, M., Oddi, S., Kruse, C., Maccarrone, M., Wadman, W., and Werkman, T. (2012). Excitability of prefrontal cortical pyramidal neurons is modulated by activation of intracellular type-2 cannabinoid receptors. Proc. Natl. Acad. Sci. U. S. A. *109*, 3534–3539.

Bouaboula, M., Bianchini, L., McKenzie, F.R., Pouyssegur, J., and Casellas, P. (1999). Cannabinoid receptor CB1 activates the Na+/H+ exchanger NHE-1 isoform via Gi-mediated mitogen activated protein kinase signaling transduction pathways. FEBS Lett. *449*, 61–65.

Brenowitz, S.D., and Regehr, W.G. (2005). Associative Short-Term Synaptic Plasticity Mediated by Endocannabinoids. Neuron *45*, 419–431.

Brusco, A., Tagliaferro, P., Saez, T., and Onaivi, E.S. (2008). Postsynaptic localization of CB2 cannabinoid receptors in the rat hippocampus. Synapse *62*, 944–949.

Buckley, N., McCoy, K., Mezey, E., Bonner, T., Zimmer, A., Felder, C., Glass, M., and Zimmer, A. (2000). Immunomodulation by cannabinoids is absent in mice deficient for the cannabinoid CB2 receptor. Eur. J. Pharmacol. *396*, 141–149.

Buzsáki, G., and Wang, X.-J. (2012). Mechanisms of Gamma Oscillations. Annu. Rev. Neurosci. *35*, 203–225.

Carta, M., Lanore, F., Rebola, N., Szabo, Z., Da Silva, S.V., Lourenço, J., Verraes, A., Nadler, A., Schultz, C., Blanchet, C., et al. (2014). Membrane Lipids Tune Synaptic Transmission by Direct Modulation of Presynaptic Potassium Channels. Neuron *81*, 787–799.

Castillo, P.E., Younts, T.J., Chávez, A.E., and Hashimotodani, Y. (2012). Endocannabinoid signaling and synaptic function. Neuron *76*, 70–81.

Chesler, M., and Kaila, K. (1992). Modulation of pH by neuronal activity. Trends Neurosci. *15*, 396–402.

Chevaleyre, V., and Castillo, P.E. (2003). Heterosynaptic LTP of Hippocampal GABAergic Synapses : A Novel Role of Endocannabinoids in Regulating Excitability. Neuron *38*, 461–472.

Chevaleyre, V., and Castillo, P.E. (2004). Endocannabinoid-Mediated Metaplasticity in the Hippocampus. Neuron *43*, 871–881.

Chevaleyre, V., Takahashi, K.A., and Castillo, P.E. (2006). Endocannabinoid-mediated synaptic plasticity in the CNS. Annu. Rev. Neurosci. *29*, 37–76.

Colgin, L.L., Denninger, T., Fyhn, M., Hafting, T., Bonnevie, T., Jensen, O., Moser, M.-B., and Moser, E.I. (2009). Frequency of gamma oscillations routes flow of information in the hippocampus. Nature *462*, 353–357.

Csicsvari, J., Jamieson, B., Wise, K.D., and Buzsáki, G. (2003). Mechanisms of Gamma Oscillations in the Hippocampus of the Behaving Rat. Neuron *37*, 311–322.

Le Duigou, C., Simonnet, J., Teleñczuk, M.T., Fricker, D., and Miles, R. (2014). Recurrent synapses and circuits in the CA3 region of the hippocampus: an associative network. Front. Cell. Neurosci. *7*:262.

Eckert, W.A., Willcockson, H.H., and Light, A.R. (2001). Interference of biocytin with opioid-evoked hyperpolarization and membrane properties of rat spinal substantia gelatinosa neurons. Neurosci. Lett. *297*, 117–120.

Galiègue, S., Mary, S., Marchand, J., Dussossoy, D., Carrière, D., Carayon, P., Bouaboula, M., Shire, D., Le Fur, G., and Casellas, P. (1995). Expression of central and peripheral cannabinoid receptors in human immune tissues and leukocyte subpopulations. Eur. J. Biochem. *232*, 54–61.

García-Gutiérrez, M.S., Ortega-Álvaro, A., Busquets, A., Pérez-Ortiz, J.M., Caltana, L., Ricatti, M.J., Brusco, A., Maldonado, R., and Manzanares, J. (2013). Synaptic plasticity alterations associated with memory impairment induced by deletion of CB2 cannabinoid receptors. Neuropharmacology *73*, 388–396.

Gerdeman, G.L., Ronesi, J., and Lovinger, D.M. (2002). Postsynaptic endocannabinoid release is critical to long-term depression in the striatum. Nat. Neurosci. *5*, 446–451.

Gong, J.-P., Onaivi, E.S., Ishiguro, H., Liu, Q.-R., Tagliaferro, P.A., Brusco, A., and Uhl, G.R. (2006). Cannabinoid CB2 receptors: immunohistochemical localization in rat brain. Brain Res. *1071*, 10–23.

Gustafsson, B., and Wigström, H. (1983). Hyperpolarization following long-lasting tetanic activation of hippocampal pyramidal cells. Brain Res. *275*, 159–163.

Hájos, N., Freund, T.F., and Freund, F. (2002). Distinct cannabinoid sensitive receptors regulate hippocampal excitation and inhibition. Chem. Phys. Lipids *121*, 73–82.

Hashimotodani, Y., Ohno-Shosaku, T., Maejima, T., Fukami, K., and Kano, M. (2008). Pharmacological evidence for the involvement of diacylglycerol lipase in depolarization-induced endocanabinoid release. Neuropharmacology *54*, 58–67.

Ho, B., Uezono, Y., Takada, S., Takase, I., and Izumi, F. (1999). Coupling of the expressed cannabinoid CB1 and CB2 receptors to phospholipase C and G Protein-coupled inwardly rectifying K+ channels. Recept. Channels *6*, 363–374.

Jenniches, I., Ternes, S., Albayram, O., Otte, D.M., Bach, K., Bindila, L., Michel, K., Lutz, B., Bilkei-Gorzo, A., and Zimmer, A. (2015). Anxiety, Stress, and Fear Response in Mice with Reduced Endocannabinoid Levels. Biol. Psychiatry, 10.1016/j.biopsych.2015.03.033.

Kaczorowski, C.C., Disterhoft, J., and Spruston, N. (2007). Stability and plasticity of intrinsic

membrane properties in hippocampal CA1 pyramidal neurons: effects of internal anions. J. Physiol. *578*, 799–818.

Kano, M., Ohno-Shosaku, T., Hashimotodani, Y., Uchigashima, M., and Watanabe, M. (2009). Endocannabinoid-Mediated Control of Synaptic Transmission. Physiol. Rev. *89*, 309–380.

Katona, I., and Freund, T.F. (2012). Multiple functions of endocannabinoid signaling in the brain. Annu. Rev. Neurosci. *35*, 529–558.

Katona, I., Sperlagh, B., Sik, A., Kafalvi, A., Vizi, E.S., Mackie, K., and Freund, T.F. (1999). Presynaptically Located CB1 Cannabinoid Receptors Regulate GABA Release from Axon Terminals of Specific Hippocampal Interneurons. J. Neurosci. *19*, 4544–4558.

Kim, J., and Alger, B.E. (2010). Reduction in endocannabinoid tone is a homeostatic mechanism for specific inhibitory synapses. Nat. Neurosci. *13*, 592–600.

Kim, J., and Li, Y. (2015). Chronic activation of CB2 cannabinoid receptors in the hippocampus increases excitatory synaptic transmission. J. Physiol. *4*, 871–886.

Kowalski, J., Gan, J., Jonas, P., and Pernia-Andrade, A.J. (2015). Intrinsic Membrane Properties Determine Hippocampal Differential Firing Pattern In Vivo in Anesthetized Rats. Hippocampus, 10.1002/hipo.22550.

Kreitzer, A.C., Carter, A.G., and Regehr, W.G. (2002). Inhibition of Interneuron Firing Extends the Spread of Endocannabinoid Signaling in the Cerebellum. Neuron *34*, 787–796.

Lee, D., Lin, B.-J., and Lee, A.K. (2012). Hippocampal place fields emerge upon single-cell manipulation of excitability during behavior. Science *337*, 849–853.

Li, Y., and Kim, J. (2015). Neuronal Expression of CB2 Cannabinoid Receptor mRNAs in the Mouse Hippocampus. Neuroscience *311*, 253–267.

Li, Y., and Kim, J. (2016). Deletion of CB2 cannabinoid receptors reduces synaptic transmission and long-term potentiation in the mouse hippocampus. Hippocampus *6*, 275–281.

Li, X., Rubio, F.J., Zeric, T., Bossert, J.M., Kambhampati, S., Cates, H.M., Kennedy, P.J., Liu, Q.-R., Cimbro, R., Hope, B.T., et al. (2015). Incubation of Methamphetamine Craving is Associated with Selective Increases in Expression of Bdnf and Grkb, Glutamate Receptors, and Epigenetic Enzymes in Cue-Activated Fos-Expressing Dorsal Striatal Neurons. J. Neurosci. *35*, 8232–8244.

Liu, Q.-R., Pan, C.-H., Hishimoto, A., Li, C.-Y., Xi, Z.-X., Llorente-Berzal, A., Viveros, M.-P., Ishiguro, H., Arinami, T., Onaivi, E.S., et al. (2009). Species differences in cannabinoid receptor 2 (CNR2 gene): identification of novel human and rodent CB2 isoforms, differential tissue expression and regulation by cannabinoid receptor ligands. Genes. Brain. Behav. *8*, 519–530.

Liu, Q.-R., Rubio, F.J., Bossert, J.M., Marchant, N.J., Fanous, S., Hou, X., Shaham, Y., and Hope, B.T. (2014). Detection of molecular alterations in methamphetamine-activated Fos-expressing neurons from a single rat dorsal striatum using fluorescence-activated cell sorting (FACS). J. Neurochem. *128*, 173–185.

Lodge, D., Tidball, P., Mercier, M.S., Lucas, S.J., Hanna, L., Ceolin, L., Kritikos, M., Fitzjohn, S.M., Sherwood, J.L., Bannister, N., et al. (2013). Antagonists reversibly reverse chemical LTD induced by group I, group II and group III metabotropic glutamate receptors.

Neuropharmacology *74*, 135–146.

Mackie, K., Lai, Y., Westenbroek, R., and Mitchell, R. (1995). Cannabinoids activate an inwardly rectifying potassium conductance and inhibit Q-type calcium currents in AtT20 cells transfected with rat brain cannabinoid receptor. J. Neurosci. *15*, 6552–6561.

Maier, N., Tejero-Cantero, A., Dorrn, A.L., Winterer, J., Beed, P.S., Morris, G., Kempter, R., Poulet, J.F.A., Leibold, C., and Schmitz, D. (2011). Coherent Phasic Excitation during Hippocampal Ripples. Neuron *72*, 137–152.

Maier, N., Morris, G., Schuchmann, S., Korotkova, T., Ponomarenko, A., Böhm, C., Wozny, C., and Schmitz, D. (2012). Cannabinoids disrupt hippocampal sharp wave-ripples via inhibition of glutamate release. Hippocampus *22*, 1350–1362.

Majumdar, D., Maunsbach, A.B., Shacka, J.J., Williams, J.B., Berger, U. V, Schultz, K.P., Harkins, L.E., Boron, W.F., Roth, K.A., and Bevensee, M.O. (2008). Localization of electrogenic Na/bicarbonate cotransporter NBCe1 variants in rat brain. Neuroscience *155*, 818–832.

Marchalant, Y., Brownjohn, P.W., Bonnet, A., Kleffmann, T., and Ashton, J.C. (2014). Validating antibodies to the cannabinoid CB2 receptor: Antibody sensitivity is not evidence of antibody specificity. J. Histochem. Cytochem. *62*, 395–404.

Marinelli, S., Pacioni, S., Cannich, A., Marsicano, G., and Bacci, A. (2009). Self-modulation of neocortical pyramidal neurons by endocannabinoids. Nat. Neurosci. *12*, 1488–1490.

Marsicano, G., Goodenough, S., Monory, K., Hermann, H., Eder, M., Cannich, A., Azad, S.C., Cascio, M.G., Gutiérrez, S.O., van der Stelt, M., et al. (2003). CB1 Cannabinoid Receptors and On-Demand Defense Against Excitotoxicity. Science *302*, 84–88.

Monory, K., Massa, F., Egertová, M., Eder, M., Blaudzun, H., Westenbroek, R., Kelsch, W., Jacob, W., Marsch, R., Ekker, M., et al. (2006). The endocannabinoid system controls key epileptogenic circuits in the hippocampus. Neuron *51*, 455–466.

Morgan, N.H., Stanford, I.M., and Woodhall, G.L. (2009). Functional CB2 type cannabinoid receptors at CNS synapses. Neuropharmacology *57*, 356–368.

Munro, S., Thomas, K.L., and Abu-Shaar, M. (1993). Molecular characterization of a peripheral receptor for cannabinoids. Nature *365*, 61–65.

Onaivi, E.S. (2006). Neuropsychobiological evidence for the functional presence and expression of cannabinoid CB2 receptors in the brain. Neuropsychobiology *54*, 231–246.

Onaivi, E.S. (2011). Commentary: Functional neuronal CB2 cannabinoid receptors in the CNS. Curr. Neuropharmacol. *9*, 205–208.

Palmer, M.J., Irving, A.J., Seabrook, G.R., Jane, D.E., and Collingridge, G.L. (1998). The group I mGlu receptor agonist DHPG induces a novel form of LTD in the CA1 region of the hippocampus. Neuropharmacology *36*, 1517–1532.

Robbe, D., Kopf, M., Remaury, A., Bockaert, J., and Manzoni, O.J. (2002). Endogenous cannabinoids mediate long-term synaptic depression in the nucleus accumbens. Proc. Natl. Acad. Sci. U. S. A. *99*, 8384–8388.

Robbe, D., Montgomery, S.M., Thome, A., Rueda-Orozco, P.E., McNaughton, B.L., and

Buzsaki, G. (2006). Cannabinoids reveal importance of spike timing coordination in hippocampal function. Nat. Neurosci. *9*, 1526–1533.

Ruffin, V.A., Salameh, A.I., Boron, W.F., and Parker, M.D. (2014). Intracellular pH regulation by acid-base transporters in mammalian neurons. Front. Physiol. *5*, 1–11.

Salter, M.W., and Beggs, S. (2014). Sublime microglia: Expanding roles for the guardians of the CNS. Cell *158*, 15–24.

Schmöle, A.-C., Lundt, R., Gennequin, B., Schrage, H., Beins, E., Krämer, A., Zimmer, T., Limmer, A., Zimmer, A., and Otte, D.-M. (2015). Expression Analysis of CB2-GFP BAC Transgenic Mice. PLoS One *10*, e0138986.

Schomburg, E.W., Fernández-Ruiz, A., Mizuseki, K., Berényi, A., Anastassiou, C.A., Koch, C., Buzsáki, G., Bere, A., Anastassiou, C.A., Schomburg, E.W., et al. (2014). Theta Phase Segregation of Input-Specific Gamma Patterns in Entorhinal-Hippocampal Networks. Neuron *84*, 470–485.

Van Sickle, M.D., Duncan, M., Kingsley, P.J., Mouihate, A., Urbani, P., Mackie, K., Stella, N., Makriyannis, A., Piomelli, D., Davison, J.S., et al. (2005). Identification and functional characterization of brainstem cannabinoid CB2 receptors. Science *310*, 329–332.

Sloviter, R.S. (1991). Permanently altered hippocampal structure, excitability, and inhibition after experimental status epilepticus in the rat: the ‘dormant basket cell’ hypothesis and its possible relevance to temporal lobe epilepsy. Hippocampus *1*, 41–66.

Sneider, J.T., Chrobak, J.J., Quirk, M.C., Tropp Sneider, J., Chrobak, J.J., Quirk, M.C., Oler, J.A., and Markus, E.J. (2006). Differential behavioral state-dependence in the burst properties of CA3 and CA1 neurons. Neuroscience *141*, 1665–1677.

Stella, N., Schweitzer, P., and Piomelli, D. (1997). A second endogenous cannabinoid that modulates long-term potentiation. Nature *388*, 773–778.

Sugiura, T., Kobayashi, Y., Oka, S., and Waku, K. (2002). Biosynthesis and degradation of anandamide and 2-arachidonoylglycerol and their possible physiological significance. Prostaglandins. Leukot. Essent. Fatty Acids *66*, 173–192.

Takahashi, K.A., and Castillo, P.E. (2006). The CB1 cannabinoid receptor mediates glutamatergic synaptic suppression in the hippocampus. Neuroscience *139*, 795–802.

Wilson, R.I., and Nicoll, R.A. (2001). Endogenous cannabinoids mediate retrograde signaling at hippocampal synapses. Nature *410*, 588–592.

Wilson, R.I., and Nicoll, R.A. (2002). Endocannabinoid signaling in the brain. Science *296*, 678–682.

Wittner, L., and Miles, R. (2007). Factors defining a pacemaker region for synchrony in the hippocampus. J. Physiol. *584*, 867–883.

Wulff, P., Ponomarenko, A.A., Bartos, M., Korotkova, T.M., Fuchs, E.C., Bähner, F., Both, M., Tort, A.B.L., Kopell, N.J., Wisden, W., et al. (2009). Hippocampal theta rhythm and its coupling with gamma oscillations require fast inhibition onto parvalbumin-positive interneurons. Proc. Natl. Acad. Sci. U. S. A. *106*, 3561–3566.

Xi, Z.-X., Peng, X.-Q., Li, X., Song, R., Zhang, H.-Y., Liu, Q.-R., Yang, H.-J., Bi, G.-H., Li, J., and Gardner, E.L. (2011). Brain Cannabinoid CB2 Receptors Modulate Cocaine's Actions in Mice. Nat. Neurosci. *14*, 1160–1166.

Young, S.R., Chuang, S.-C., Zhao, W., Wong, R.K.S., and Bianchi, R. (2013). Persistent receptor activity underlies group I mGluR-mediated cellular plasticity in CA3 neuron. J. Neurosci. *33*, 2526–2540.

Younts, T.J., Chevaleyre, V., and Castillo, P.E. (2013). CA1 Pyramidal Cell Theta-Burst Firing Triggers Endocannabinoid-Mediated Long-Term Depression at Both Somatic and Dendritic Inhibitory Synapses. J. Neurosci. *33*, 13743–13757.

Zhang, H.-Y., Gao, M., Liu, Q.-R., Bi, G.-H., Li, X., Yang, H.-J., Gardner, E.L., Wu, J., and Xi, Z.-X. (2014). Cannabinoid CB 2 receptors modulate midbrain dopamine neuronal activity and dopamine-related behavior in mice. Proc. Natl. Acad. Sci. *111*, E5007–E5015.

Zimmer, A., Zimmer, A., Hohmann, A.G., Herkenham, M., and Bonner, T.I. (1999). Increased mortality, hypoactivity, and hypoalgesia in cannabinoid CB1 receptor knockout mice. Proc. Natl. Acad. Sci. U. S. A. *96*, 5780–5785.

Figure legends

Figure 1. Action potential firing induces a cell type-specific V_m hyperpolarization in hippocampal principal cells. (**A-C**) Current injection-triggered AP trains (rectangle) induce a long-lasting V_m hyperpolarization in CA3 PCs (A) but not in CA1 PCs (B) and DG GCs (C). Left: exemplary pp recordings of each principal cell population. APs have been truncated and test pulses cut for display purposes in this and all later figures. Insets: firing patterns (scale bar: 40mV, 0.2s). Right: summary time course of the ΔV_m average for CA3 PCs: n(N)=17(13), CA1 PCs: n(N)=14(4) and DG GCs: n(N)=8(4). The x-axis is discontinued for the duration of the AP train. (**D**) The ΔV_m of each recorded cell (circles) and the median, 25th and 75th percentile of the average ΔV_m calculated from the first minute after the last AP train are shown for CA3 PCs (-4.1, -5.4 and -3.6mV), CA1 PCs (0.30, -0.15 to 0.68mV) and DG GCs (1.04, -0.35 to 1.8mV). Kruskal-Wallis with Dunn's post-test: $p<0.05$ for CA3 PCs vs. CA1 PCs and DG GCs. (**E**) Percentage (%) reactive cells.

Figure 2. The eCB 2-AG mediates the hyperpolarization. (**A**) As a control, sIPSCs were recorded from WT and DAGLα$^{-/-}$ CA3 PCs to test for the presence of DSI. In contrast to a DSI+ WT CA3 PC (upper trace), depolarization of a DAGLα$^{-/-}$ CA3 PC (0mV for 3x1s) failed to induce DSI (lower trace). (**B**) The normalized change in amplitude (left) and frequency (right) of sIPSCs in DAGLα$^{-/-}$ CA3 PCs (n(N)=3(1): 1.4±0.17 and 1.2±0.05) differed significantly from WT controls (n(N)=5(1)), 0.55±0.1 and 0.78±0.1, Mann-Whitney test: P=0.036). The absolute sIPSC amplitude and frequency after DSI induction in the DAGLα KO do not differ from baseline (Wilcoxon test: P=0.25). (**C**) Example V_m response of a DAGLα$^{-/-}$ CA3 PC to the AP stimulus (rectangle). (**D**) Left: the ΔV_m of each recorded cell (circles) and the median, 25th and 75th percentile of the average ΔV_m are shown for n(N)=6(3) experiments in pp (-0.2, -0.7 and 1.5mV; Wilcoxon test: P=0.84 in comparison to baseline). Right: % reactive cells. For statistical comparison, the V_m values from WT CA3 PCs (Figure 1) are re-plotted in grey (Mann Whitney test: $p<0.0001$).

Figure 3. The long-lasting hyperpolarization is absent in CB_2R-deficient mice. (**A-C**) AP trains (rectangle) induce a long-lasting hyperpolarization in $CB_1R^{-/-}$ CA3 PCs (A) but not in CA3 PCs of $CB_2R^{-/-}$ (B) and Syn-$CB_2R^{-/-}$ mice (C). Left: exemplary pp recordings of KO CA3 PCs. Right: summary time course of the average ΔV_m of CA3 PCs recorded from $CB_1R^{-/-}$: n(N)=8(6), $CB_2R^{-/-}$: n(N)=15(7) and Syn-$CB_2R^{-/-}$: n(N)=8(5). The x-axis is discontinued for the duration of the AP train. (**D**) Same as (A-C) for WT littermate controls of $CB_2R^{-/-}$ and Syn-$CB_2R^{-/-}$ mice: n(N)=4(3)/4(2). (**E**) The ΔV_m of each recorded cell (circles) and the median, 25th and 75th percentile of the average ΔV_m (min9-10) are shown for CA3 PCs recorded in $CB_1R^{-/-}$ (-4.3, -5.8 and -2.6mV), (Syn-)$CB_2R^{+/+}$ littermates (-4.7, -5.8 to -3.5mV), $CB_2R^{-/-}$ (0.39, -0.57 to 1.4mV) and Syn-$CB_2R^{-/-}$ (0.53, 0.086 to 1.1mV). Kruskal-Wallis with Dunn's post test: $p<0.0001$ for [WT and $CB_1R^{-/-}$] vs. [$CB_2R^{-/-}$ and Syn-$CB_2R^{-/-}$]. The average ΔV_m of WT vs. $CB_1R^{-/-}$ and $CB_2R^{-/-}$ vs. Syn-$CB_2R^{-/-}$ did not differ significantly. (**F**) % reactive cells.

Figure 4. Neuronal CB_2R mRNA expression in the hippocampus by RNAscope ISH and FACS-qPCR assays. (**A**) Hippocampal image (DAPI staining), illustrating the target region (CA3) in C. (**B**) The CB_2R mRNA structure in CB_2R-floxed mice and the target gene region of a CB_2R RNAscope probe (CB_2-O2, 506-934bp) used to detect CB_2R mRNA. The CB_2-O2 probe targets the floxed region of mouse CB_2R mRNA (NM_009924.4) in CB_2R-floxed mice. CDS, (CB_2R)-coding DNA sequence (478-1521bp). (**C**) CB_2R mRNA staining illustrating significant CB_2R (*Cnr2*, green) and NeuN (*Rbfox,* red) mRNA co-localization in WT hippocampal CA3 neurons (upper panels), while such co-localization is substantially diminished in Syn-$CB_2R^{-/-}$ (lower panels). (**D**) A representative image of FACS-sorted NeuN+ neurons and NeuN- non-neuronal cells in the

hippocampus. (**E**) qPCR assays show that CB_2R mRNA is detected mainly in NeuN+ hippocampal cells of WT mice, while the CB_2R mRNA in NeuN+ hippocampal cells in Syn-$CB_2R^{-/-}$ mice was substantially reduced (~70% reduction), and abolished in the $CB_2R^{-/-}$ mice. (**F**) qPCR assays for CB_1R mRNA (as controls) in the same samples demonstrate similar levels of CB_1R mRNA expression in NeuN+ neurons and NeuN- cells in WT, Syn-$CB_2R^{-/-}$ and const. $CB_2R^{-/-}$ mice. (**G**) qPCR assay results of neuronal and glial markers in two cell populations to examine the purity of sorted cells, illustrating that *Rbfox3* was detected mainly in FACS-sorted NeuN+ neurons (a), but not in NeuN- cells (b). In contrast, the glial marker genes *Itgam*, *Cspg4* and *Aldh1l1* were mainly detected in NeuN- non-neuronal cells (b), but not in NeuN+ hippocampal neurons (a). Data shown in (a) was normalized to *Rbfox3* expression in the NeuN+ population, which was defined as 1. Data shown in (b) was normalized to each respective marker gene level in NeuN+ (*Rbfox3*) and NeuN- cells (all three glial markers).

Figure 5. CB_2R agonists mimic and occlude the AP-driven hyperpolarization. (**A-D**) Exemplary V_m time courses of wc CA3 PC recordings are shown for the application of 10µM 2-AG (A), 1µM WIN (B) and 1µM HU (C) that hyperpolarise CA3 PCs. The hyperpolarising effect of HU is gone in the $CB_2R^{-/-}$ (D). (**E-F**) The ΔV_m of each recorded cell (circles) and the median, 25thand 75th percentile of the average ΔV_m (E) as well as the % of reactive cells (F) are shown for the application of 2-AG in WT (wc, n(N)=15(5): -5.3, -9.0 to -3.9mV; 53.3%) and in $CB_2R^{-/-}$ (pp, n(N)=5(2): 1.6, 0.5 to 2.2mV; 0%), WIN in WT (wc, n(N)=23(15): -4.2, -5.6 to -2.7mV; 60.9%), HU in WT (wc, n(N)=20(10): -7.6, -9.7 to -4.9mV; 60%), HU in $CB_2R^{-/-}$ (wc, n(N)=12(3): 0.9, 0.3 to 1.5mV; 8.3%), HU in Syn-$CB_2R^{-/-}$ (wc, n(N)=14(5): 1.4, 0.3 to 3mV, 0%) and HU in Syn-$CB_2R^{+/+}$ (wc, n(N)=6(4): -7.5, -9 to -5.7mV; 50%). Note that the filled circles indicate reactive cells. Colour code: 2-AG/green, WIN/yellow and HU/blue. Kruskal-Wallis with Dunn's post-test: $p<0.05$ for 2-AG and HU in $CB_2R^{-/-}$ vs. WT. (**G**) AM-251 reverses the hyperpolarization induced by 2-AG in n(N)=3(3) CA3 PCs (-5.3±0.9mV and -0.9±1mV respectively). (**H**) The HU-induced hyperpolarization (blue line) occludes further hyperpolarization of CA3 PCs in response to APs (rectangle) and vice versa. Exemplary ΔV_m time courses of CA3 PCs that hyperpolarise in response to HU (left) and AP trains (right). (**I**) Single occlusion experiments (grey circles) and mean±SEM (black) are shown for each condition. Average ΔV_m for HU followed by APs (left, n(N)=6(4): -6.6±1.3 and -7.8±1.9mV, paired t-test: P=0.24) and APs followed by HU (right, n(N)=6(6): -4.2±1.2 and -3.4±0.9mV, P=0.19).

Figure 6. The hyperpolarization is mediated by a G Protein- and Na^+-dependent modulation of the NBC. (**A**) Exemplary ΔV_m time courses of wc CA3 PC recordings with internal application of 0.5mM GDPßS. The subsequent application of 1µM HU fails to hyperpolarise the CA3 PC. (**B**) The ΔV_m of each recorded cell (circles) and the median, 25th and 75th percentile of the average ΔV_m (left) as well as the % of reactive cells (right) are shown for GDPßS+HU (n(N)=15(5): 0.6, -0.04 and 3.6mV; 13.3%) and are significantly different from control WT cells (ΔV_m: $p<0.0001$, compare to Figure 5E). Note that the remaining reactive cells (indicted by filled circles) are most likely caused by an insufficient diffusion of GDPßS given the short incubation of 5min to prevent washout. (**C**) Exemplary V_m traces of reactive CA3 PCs recorded in wc configuration that hyperpolarized in response to 10µM 2-AG (left), 1µM WIN (middle) and 1µM HU (right). The R_{in} was calculated from the steady-state response to a -80pA test pulse. In each panel, the left trace represents the control condition (1min before agonist application) and the right trace is taken from 5-10min after the drug was bath applied. The respective V_m values are indicated below each trace. (**D**) Summary bar graph of all reactive cells showing the normalized ΔR_{in} (mean±SEM) after drug application for 2-AG (n=8: 1.1±0.1), WIN (n=14: 1.01±0.05) and HU (n=12: 1.2±0.1) that do not differ significantly from baseline levels (paired t-test for 2-AG, WIN and HU: P=0.30, 0.99 and

0.12). (**E**) IV plot of n(N)=4(2) reactive CA3 PCs that were recorded at different holding potentials in voltage clamp (-110 to 40mV, 10mV steps) before and after the application of HU. The hyperpolarization was not accompanied by a change in the IV relationship (normalized to -60mV, paired t-test: P=0.66). (**F-H**) Replacement of Na^+ with NMDG in the ACSF as well as block of the NBC by preincubation of the antagonist S0859 abolished the hyperpolarization. Examples of ΔV_m values for the application of HU in NMDG (D), HU in S0859 (E), and AP stimulation in S0859 in CA3 PCs (F). (**I**) The ΔV_m of each recorded cell (circles) and the median, $25^{th}$and 75^{th} percentile of the average ΔV_m (left) as well as the % of reactive cells (right) are shown for the application of HU in NMDG (wc, n(N)=11(5): 1.9, -1.1 to 2.8mV; 0%), HU in S0859 (wc, n(N)=16(6): 0.01, -1.1 to 1.7mV, 6.25%), APs in S0859 (wc, n(N)=23(9): 1.1, 0.1 to 3mV, 4.3%) and, as a control, HU in 10µM ouabain (wc, n(N)=17(6), -5.8, -7.9 to -4.2mV, 52.9%).

Figure 7. Comparison of CB_2R- vs. presynaptic CBR-mediated effects. (A,B) The continuous block of glutamatergic (20µM NBQX, 50µM D-AP5) as well as GABAergic (1µM Gabazine, 1µM CGP) transmission does not abolish the AP-induced hyperpolarization. (**A**) Example wc recording of a reactive CA3 PC in response to the AP train (rectangle). (**B**) The ΔV_m of each recorded cell (circles) and the median, 25^{th} and 75^{th} percentile of the average ΔV_m of all reactive cells is shown for n(N)=8(2) experiments (-4.8, -8.3 and -3.8mV; left). The % of reactive cells is 62.5% (right). (**C**) Dual pp recording of 2 CA3 PCs. AP firing in a control cell (lower trace) elicits a hyperpolarization in this, but not in the other cell (upper trace). The AHPs of the control cell are clipped for display purposes. (**D**) In 5/5 recordings (N=5), the control cell hyperpolarized in response to the AP trains (filled grey circles, ΔV_m: -6.0±1.5mV), whereas the unstimulated cell did not (open black circles, ΔV_m: 0.02±0.6mV). (**E-F**) CB_2R agonists cannot mimic CB_1R-mediated depression of synaptic transmission. (**E**) HU has no effect on DSI-positive eIPSCs. Left: example of a CA3 PC recorded in wc configuration. Depolarization of the neuron results in a transient reduction of eIPSC amplitude, whereas bath application of HU does not. Right: mean normalized eIPSC amplitudes of n(N)=5(4) experiments for DSI (0.7±0.03) and HU application (1±0.05) in comparison to baseline (paired t-test: P=0.0016 and P=0.67). (**F**) WIN, but not HU, suppresses evoked field responses in CA3. Left: exemplary fEPSP recording with HU and WIN bath application. Right: mean normalized fEPSP slopes for HU (1±0.03) and WIN (0.7±0.05) in comparison to baseline (paired t-test: P=0.33 and p<0.001).

Figure 8. Functional relevance of CB_2R activation probed *in vitro* and *in vivo*.
(**A-C**) Physiological spike trains trigger long-lasting hyperpolarization. (**A**) Schematic of the presented PST (upper panel) as well as a segment of an exemplary V_m trace of a rat CA3 PC that fires in response to the respective stimulus (lower panel). (**B**) V_m time plot of the same CA3 PC responding to the PST (rectangle) with a long-lasting hyperpolarization. (**C**) Left: the ΔV_m of each recorded cell (circles) and the median, 25^{th} and 75^{th} percentile of the average ΔV_m of reactive rat CA3 PCs (wc, n(N)=16(6): -4.5, -6.7 and -2.7mV). Right: % of reactive cells (50%).
(**D-F**) CB_2R activation reduces the spike probability of CA3 PCs. (**D**) The spike probability of a CA3 PC in response to the application of the CB_2R agonist HU. Example traces show spikes elicited by synaptic stimulation during control conditions (black) and 5min after HU application (red). The baseline and hyperpolarized V_m values are indicated below the traces. (**E**) Time plot of the V_m (circles) of the same cell and its AP firing (vertical lines) for each given V_m. (**F**) Summary graph of the spike probability for n(N)=5(3) reactive cells under baseline and agonist conditions (0.8±0.02 and 0.14±0.04 respectively). The change in spike probability was accompanied by an average V_m hyperpolarization of -6.3±0.3mV.
(**G-H**) CB_2Rs regulate hippocampal gamma oscillations *in vivo*: altered coupling of gamma and theta oscillations after HU application. (**G**) LFP signal traces (1-150Hz band-pass filtered) recorded in the CA3 area during exploratory behavior before (upper panel) and 30min after (lower panel) the i.p. administration of HU (10mg/kg). Note that the typical association of high amplitude

gamma oscillations with theta oscillation peaks (shades) and low amplitude gamma oscillations with theta oscillation troughs is altered after the CB_2R agonist administration. (**H**) The theta modulation of slow (30-85Hz) but not intermediate (65-120Hz) gamma oscillations was reduced by the agonist administration (vehicle: n(N)=15(10), agonist: n(N)=13(10), $F_{1,13}$=9.1, P=0.010, slow, $F_{1,13}$=0.0, P=0.86, ANOVA).

Figure 1

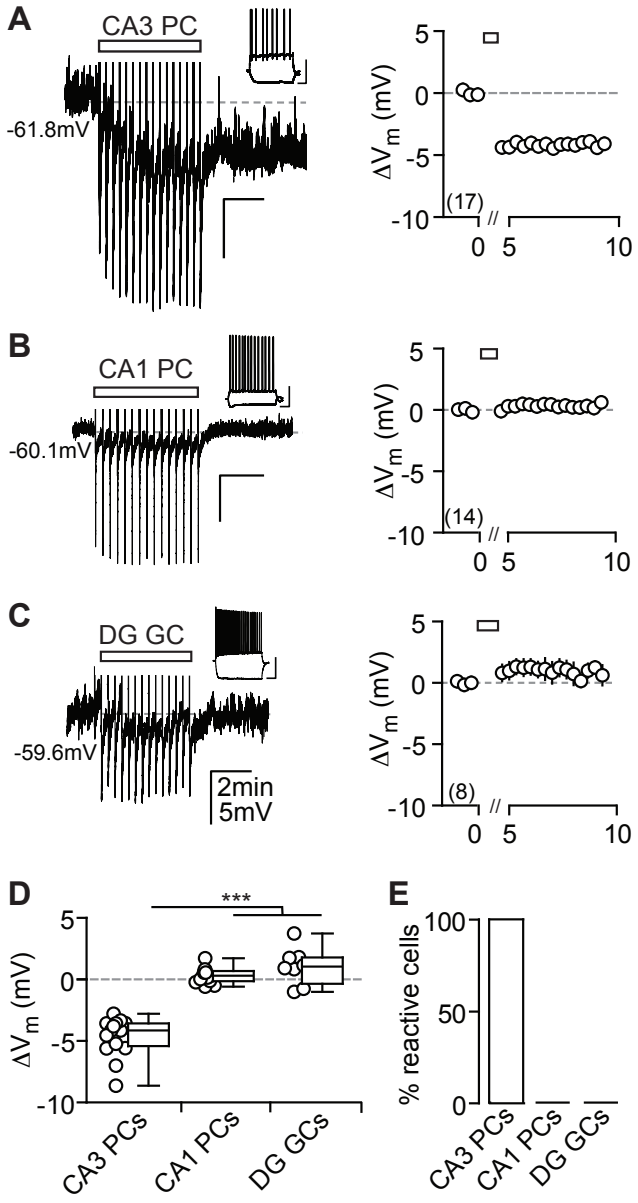
A
CA3 PC
-61.8mV
5
0
-5
-10
ΔVm (mV)
(17)
0 5 10
B
CA1 PC
-60.1mV
(14)
C
DG GC
-59.6mV
2min
5mV
(8)
D
***
CA3 PCs
CA1 PCs
DG GCs
E
100
50
0
% reactive cells

Figure 2

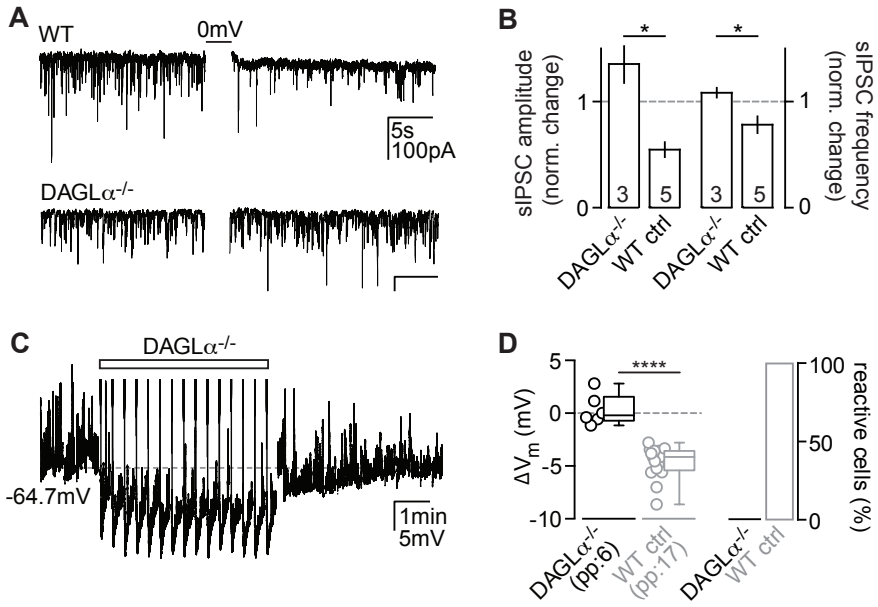
A
WT
0mV
5s
100pA
DAGLα-/-
B
sIPSC amplitude (norm. change)
sIPSC frequency (norm. change)
*
*
1
0
3
5
3
5
DAGLα-/-
WT ctrl
DAGLα-/-
WT ctrl
C
DAGLα-/-
-64.7mV
1min
5mV
D
ΔVm (mV)
5
0
-5
-10
****
100
50
0
reactive cells (%)
DAGLα-/- (pp:6)
WT ctrl (pp:17)
DAGLα-/-
WT ctrl

Figure 3

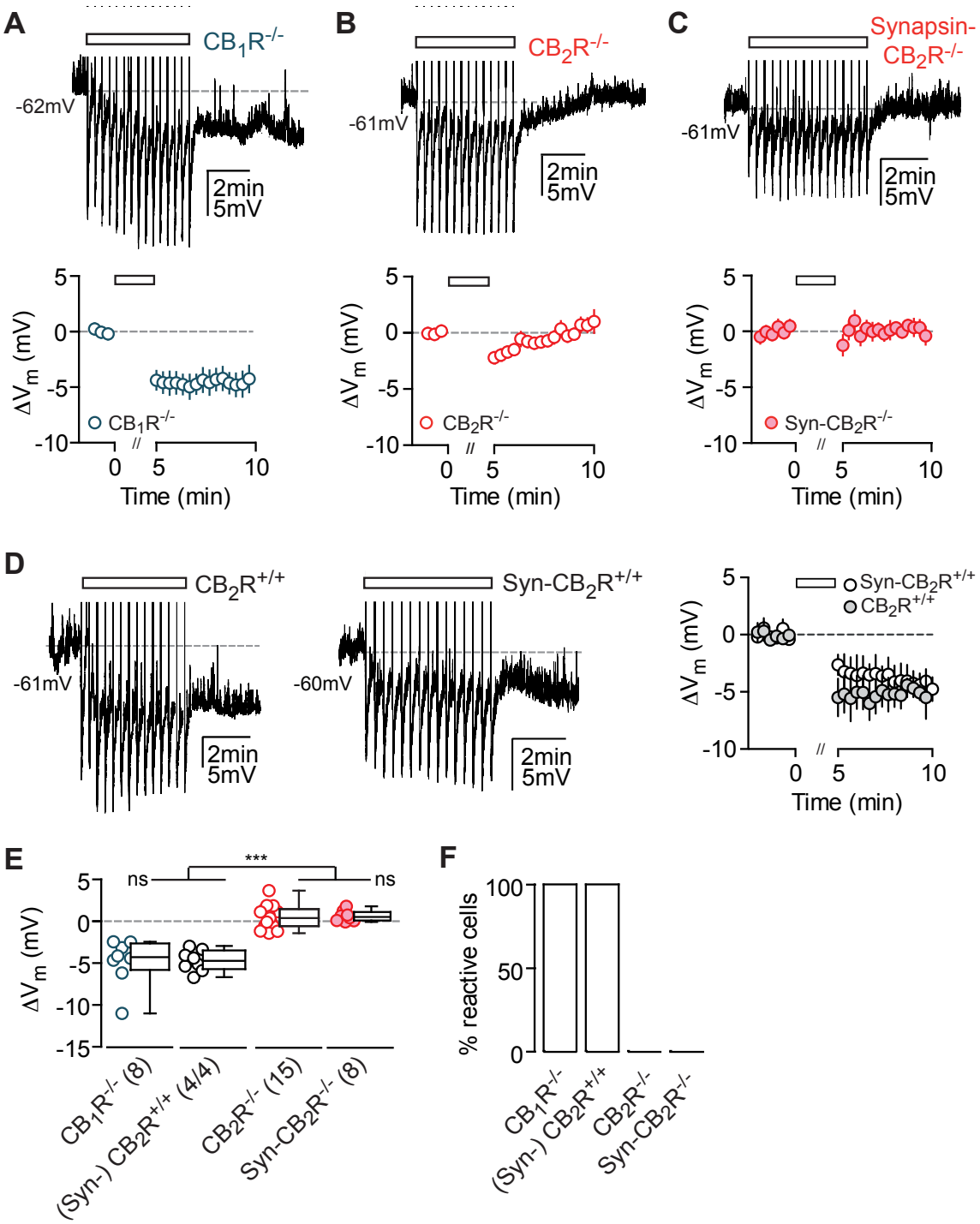
A
CB1R-/-
-62mV
2min
5mV
ΔVm (mV)
CB1R-/-
Time (min)
B
CB2R-/-
-61mV
2min
5mV
ΔVm (mV)
CB2R-/-
Time (min)
C
Synapsin-
CB2R-/-
-61mV
2min
5mV
ΔVm (mV)
Syn-CB2R-/-
Time (min)
D
CB2R+/+
-61mV
2min
5mV
Syn-CB2R+/+
-60mV
2min
5mV
Syn-CB2R+/+
CB2R+/+
ΔVm (mV)
Time (min)
E
ns
***
ns
ΔVm (mV)
CB1R-/- (8)
(Syn-) CB2R+/+ (4/4)
CB2R-/- (15)
Syn-CB2R-/- (8)
F
% reactive cells
CB1R-/-
(Syn-) CB2R+/+
CB2R-/-
Syn-CB2R-/-

Figure 4

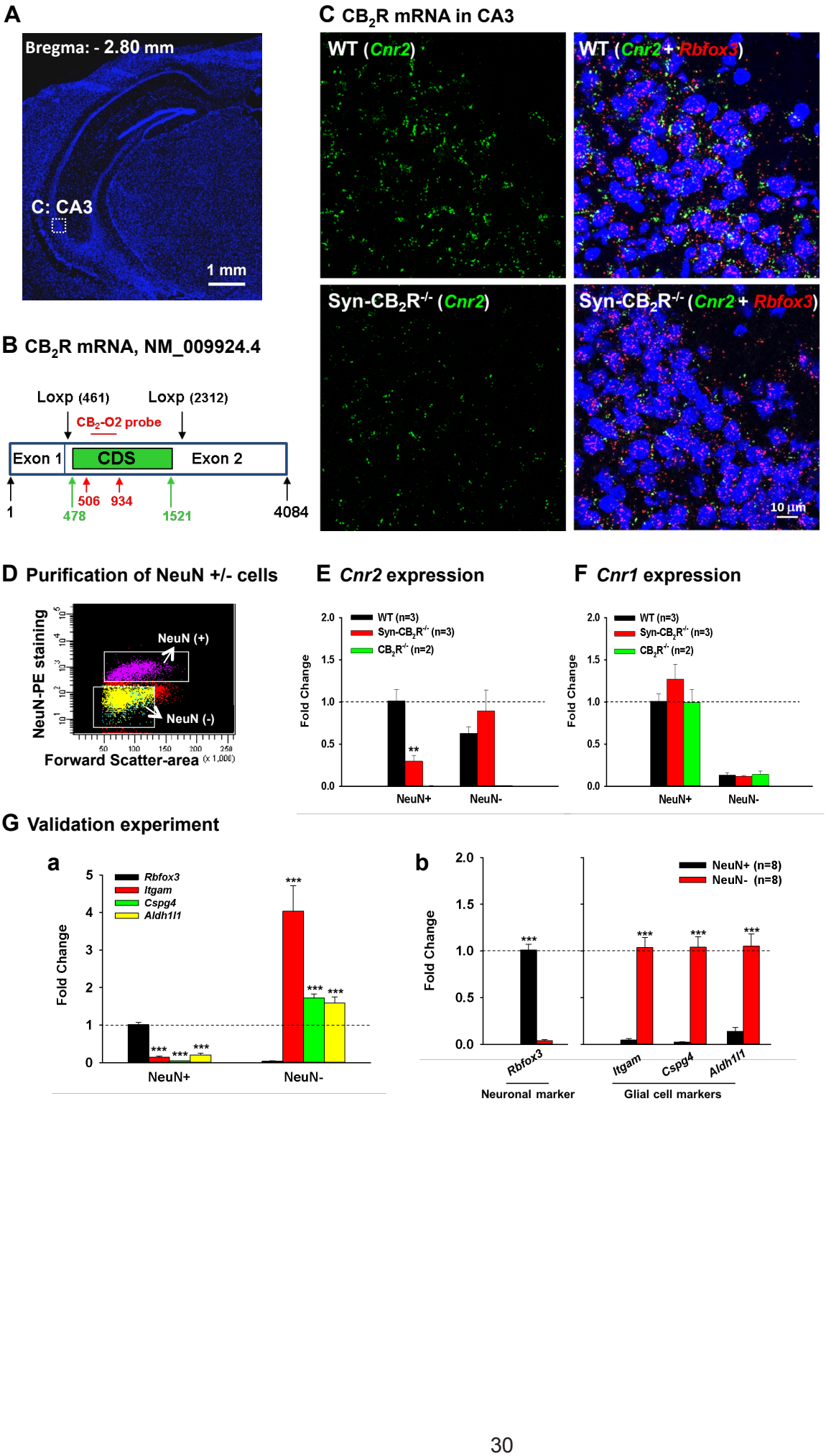
A
Bregma: - 2.80 mm
C: CA3
1 mm
B CB2R mRNA, NM_009924.4
Loxp (461)
Loxp (2312)
CB2-O2 probe
Exon 1
CDS
Exon 2
1
478
506
934
1521
4084
C CB2R mRNA in CA3
WT (Cnr2)
WT (Cnr2 + Rbfox3)
Syn-CB2R-/- (Cnr2)
Syn-CB2R-/- (Cnr2 + Rbfox3)
10 µm
D Purification of NeuN +/- cells
NeuN-PE staining
NeuN (+)
NeuN (-)
Forward Scatter-area (x 1,000)
E Cnr2 expression
F Cnr1 expression
WT (n=3)
Syn-CB2R-/- (n=3)
CB2R-/- (n=2)
Fold Change
NeuN+
NeuN-
G Validation experiment
a
Rbfox3
Itgam
Cspg4
Aldh1l1
b
NeuN+ (n=8)
NeuN- (n=8)
Neuronal marker
Glial cell markers

Figure 5

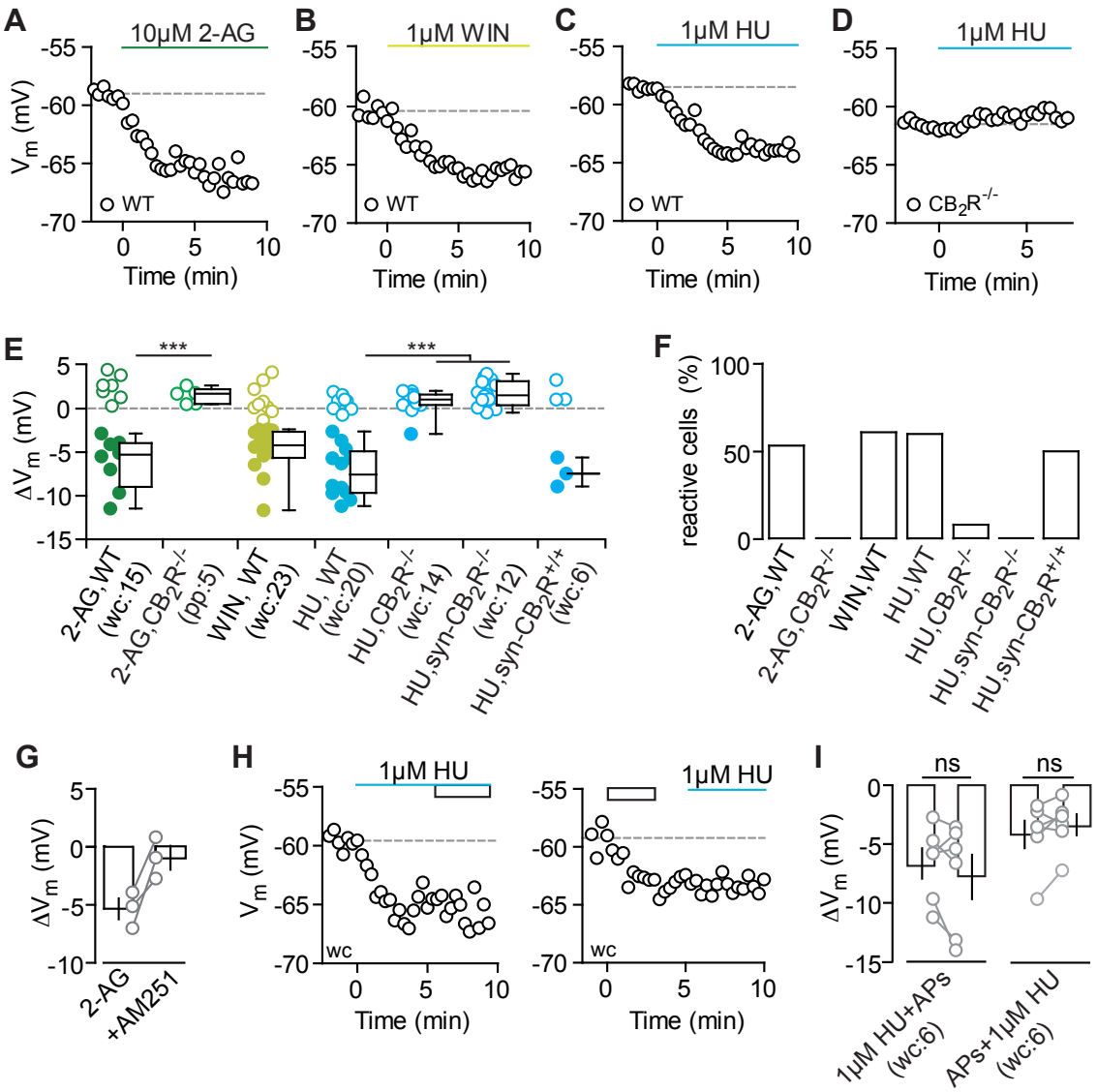
A
10µM 2-AG
B
1µM WIN
C
1µM HU
D
1µM HU
WT
WT
WT
CB2R-/-
Vm (mV)
Time (min)
E
ΔVm (mV)
***
***
2-AG,WT (wc:15)
2-AG,CB2R-/- (pp:5)
WIN, WT (wc:23)
HU, WT (wc:20)
HU,CB2R-/- (wc:14)
HU,syn-CB2R-/- (wc:12)
HU,syn-CB2R+/+ (wc:6)
F
reactive cells (%)
G
ΔVm (mV)
2-AG
+AM251
H
1µM HU
1µM HU
wc
wc
Vm (mV)
Time (min)
I
ns
ns
ΔVm (mV)
1µM HU+APs (wc:6)
APs+1µM HU (wc:6)

Figure 6

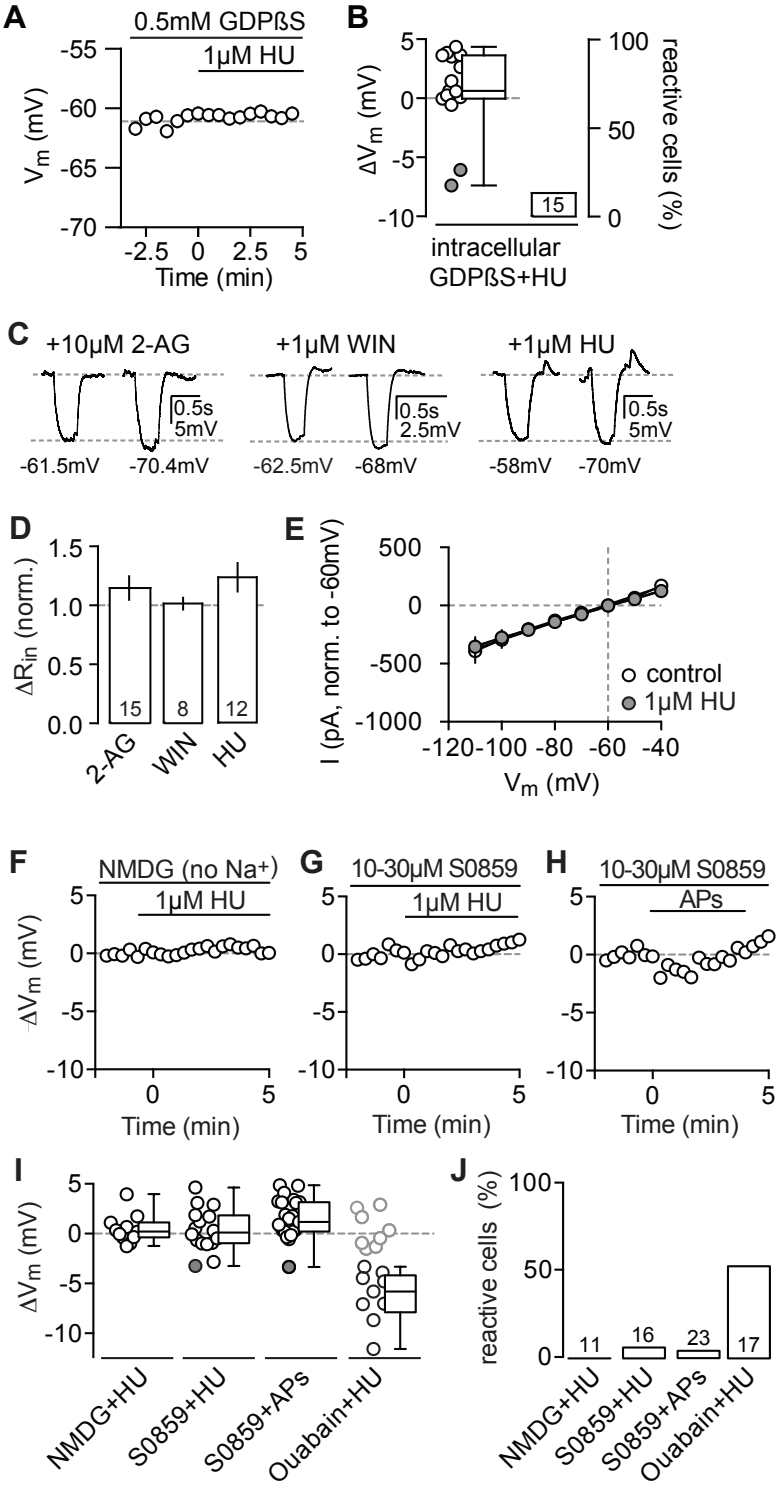
A
0.5mM GDPßS
1µM HU
-55
-60
-65
-70
V_m (mV)
-2.5 0 2.5 5
Time (min)
B
5
0
-5
-10
ΔV_m (mV)
100
50
0
reactive cells (%)
15
intracellular
GDPßS+HU
C
+10µM 2-AG
+1µM WIN
+1µM HU
0.5s
5mV
0.5s
2.5mV
0.5s
5mV
-61.5mV
-70.4mV
-62.5mV
-68mV
-58mV
-70mV
D
1.5
1.0
0.5
0.0
ΔR_{in} (norm.)
15
8
12
2-AG
WIN
HU
E
500
0
-500
-1000
I (pA, norm. to -60mV)
control
1µM HU
-120 -100 -80 -60 -40
V_m (mV)
F
NMDG (no Na+)
1µM HU
5
0
-5
-10
ΔV_m (mV)
0
5
Time (min)
G
10-30µM S0859
1µM HU
0
5
Time (min)
H
10-30µM S0859
APs
0
5
Time (min)
I
5
0
-5
-10
ΔV_m (mV)
NMDG+HU
S0859+HU
S0859+APs
Ouabain+HU
J
100
50
0
reactive cells (%)
11
16
23
17
NMDG+HU
S0859+HU
S0859+APs
Ouabain+HU

Figure 7

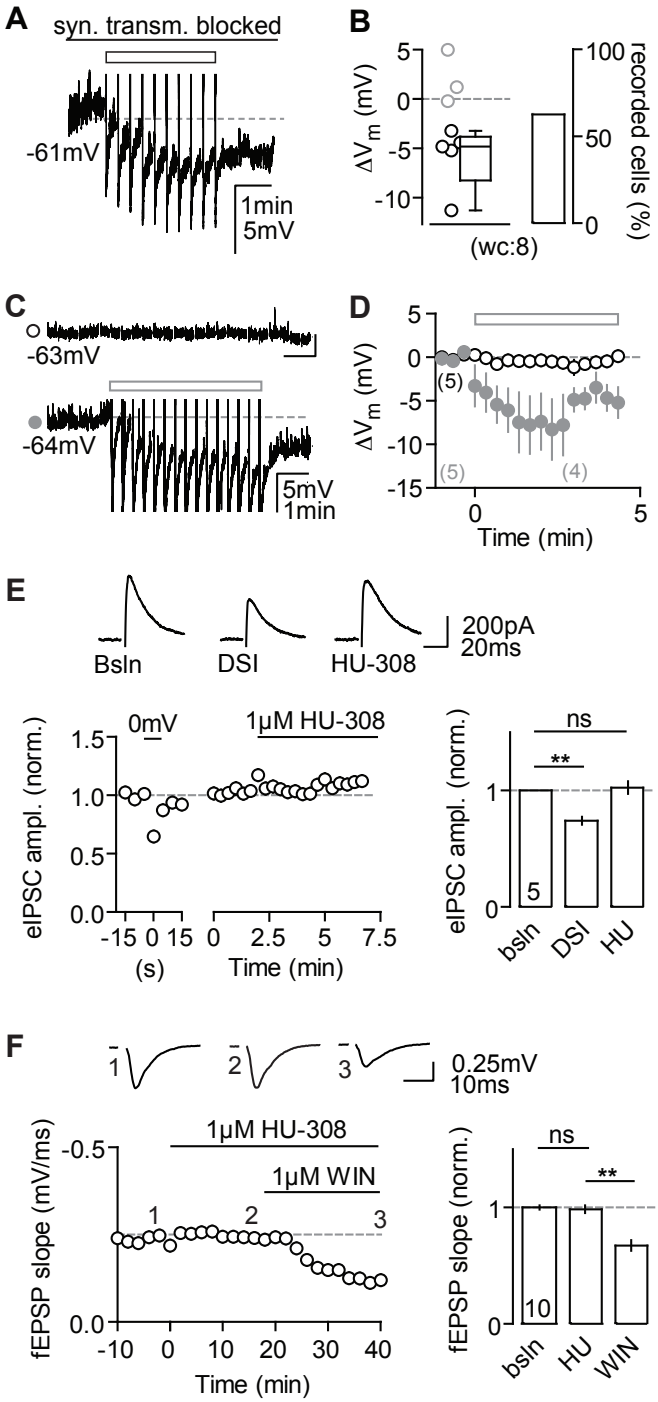
A
syn. transm. blocked
-61mV
1min
5mV
B
ΔVm (mV)
recorded cells (%)
(wc:8)
C
-63mV
-64mV
5mV
1min
D
ΔVm (mV)
(5)
(5)
(4)
Time (min)
E
Bsln
DSI
HU-308
200pA
20ms
eIPSC ampl. (norm.)
0mV
1μM HU-308
(s)
Time (min)
ns
**
bsln
DSI
HU
F
0.25mV
10ms
fEPSP slope (mV/ms)
1μM HU-308
1μM WIN
Time (min)
fEPSP slope (norm.)
bsln
HU
WIN

Figure 8

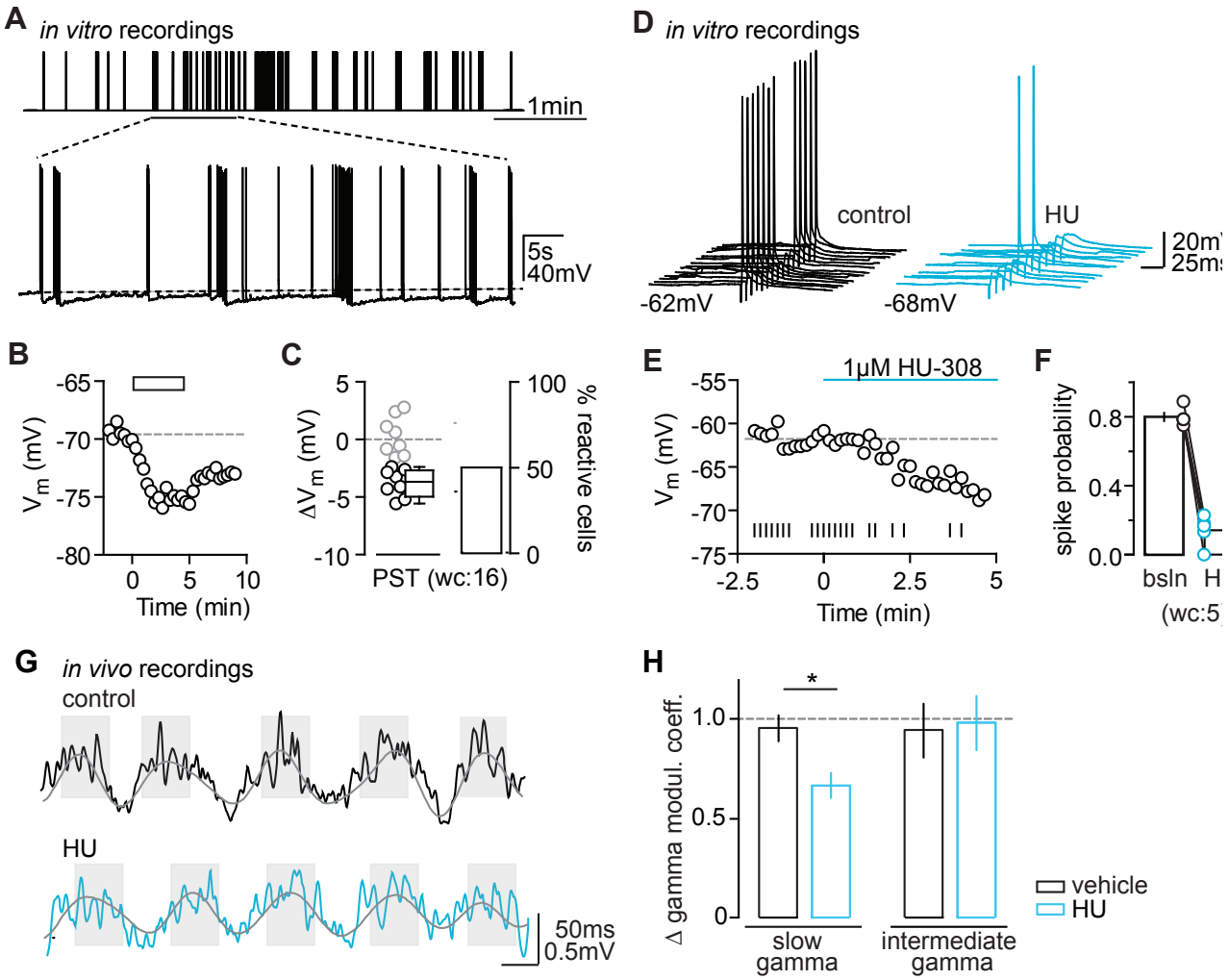
A
in vitro recordings
1min
5s
40mV
D
in vitro recordings
control
HU
-62mV
-68mV
B
C
E
1μM HU-308
F
Vm (mV)
ΔVm (mV)
% reactive cells
PST (wc:16)
Time (min)
spike probability
bsln
G
in vivo recordings
control
HU
50ms
0.5mV
H
Δ gamma modul. coeff.
slow gamma
intermediate gamma
vehicle
HU

Supplemental Materials

Supplemental Figures

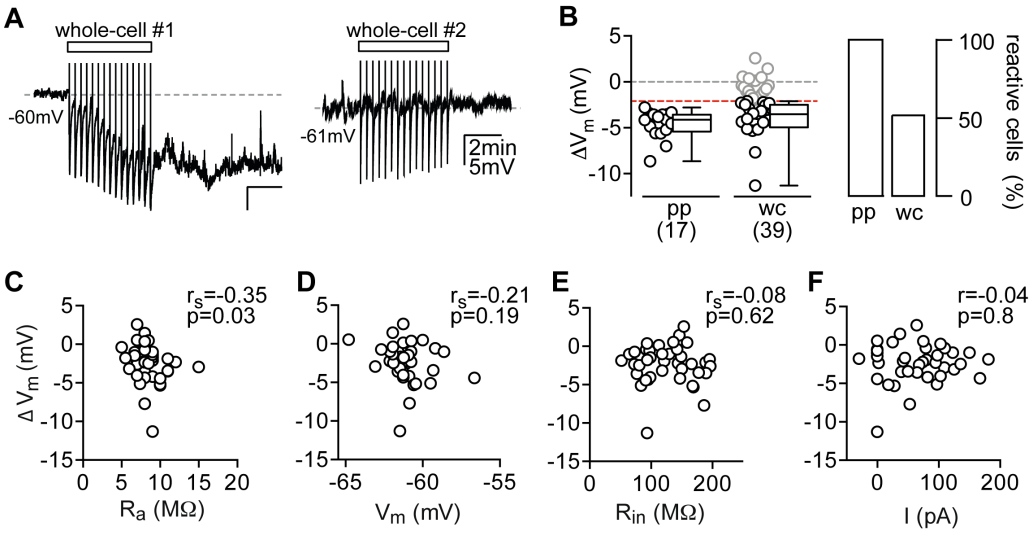

Figure S1. Related to Figure 1. Whole-cell recordings interfere with the V_m hyperpolarisation. (**A**) Whole-cell current-clamp recording of a reactive (left) and an unreactive CA3 PC (right) in response to the AP train stimulus (rectangle). (**B**) Left: the ΔV_m of each recorded cell (open circles) and the median, 25th and 75th percentile of the average ΔV_m recorded in the different recording conditions are shown for pp (data as in Fig. 1) and for n(N)=39(16) wc recordings (wc, with n=20 reactive cells: -3.5, -4.9 and -2.5mV). The dashed red line indicates the cut-off of -2.1mV by which cells were classified as reactive (black circles) or unreactive (grey circles). Right: % of reactive cells is shown for pp (100%) and wc (51.2%) recordings. (**C-F**) Correlation analysis of the ΔV_m and recording variables: The ΔV_m was significantly correlated to the R_a (C) but not the R_{in} (D), V_m (E) and the constant current injection needed to keep the cell at a holding potential of -60mV (F). Both the correlation coefficient (r or r_s) and the correlation's significance (p) are given for each correlation.

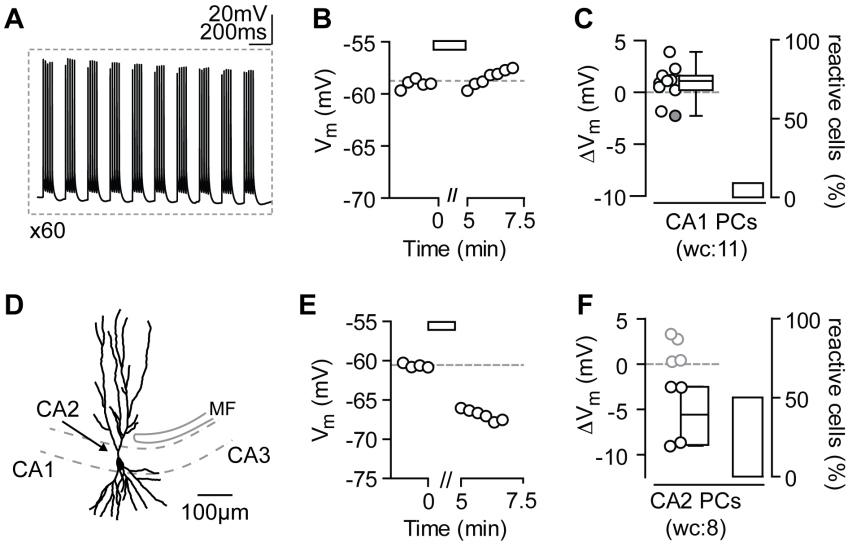

Figure S2. Related to Figure 1. Further analysis of cell-type specificity. (**A-C**) A theta-frequency burst protocol was used to elicit a total of 3000 action potentials in CA1 PCs recorded in wc configuration**.** (**A**) The first ten bursts in a recorded CA1 PCs are shown that were repeated 60x over 5 min. (**B**) The complete induction protocol (rectangle) did not induce a long-lasting hyperpolarisation in the same CA1 PC as can be seen in the time plot of its V_m. The V_m during the induction protocol is not included for display purposes. (**C**) Summary plot of n(N)=11(2) CA1 PCs with a ΔV_m (median, 25th and 75th percentile) of 1.12, 0.22 and 1.63mV (Wilcoxon test: P=0.64 compared to baseline). (**D-F**) CA2 PCs display a hyperpolarisation that is similar to CA3 PCs. (**D**) Anatomical reconstruction of a CA2 PC filled with 30µM Alexa. Note the characteristic bifurcation of the proximal dendritic tree (indicated by black arrow). The pyramidal cell layer is indicated by the dashed lines and the axonal projections from DG GCs, the mossy fibres (MF) that end at the border of CA3 to CA2, are shown in grey. (**E**) Time plot of the V_m of the same CA2 PC as in (D) in response to the action potential protocol (rectangle) recorded in wc configuration. The dashed line indicates the average baseline V_m. (**F**) The ΔV_m of each recorded cell (circles) and the median, 25th and 75th percentile of the average ΔV_m of all reactive cells are shown for (n(N)=8(5)) CA2 PCs: -5.8, -8.9 and -2.5mV (left). The percentage of reactive CA2 PCs was 50% (right).

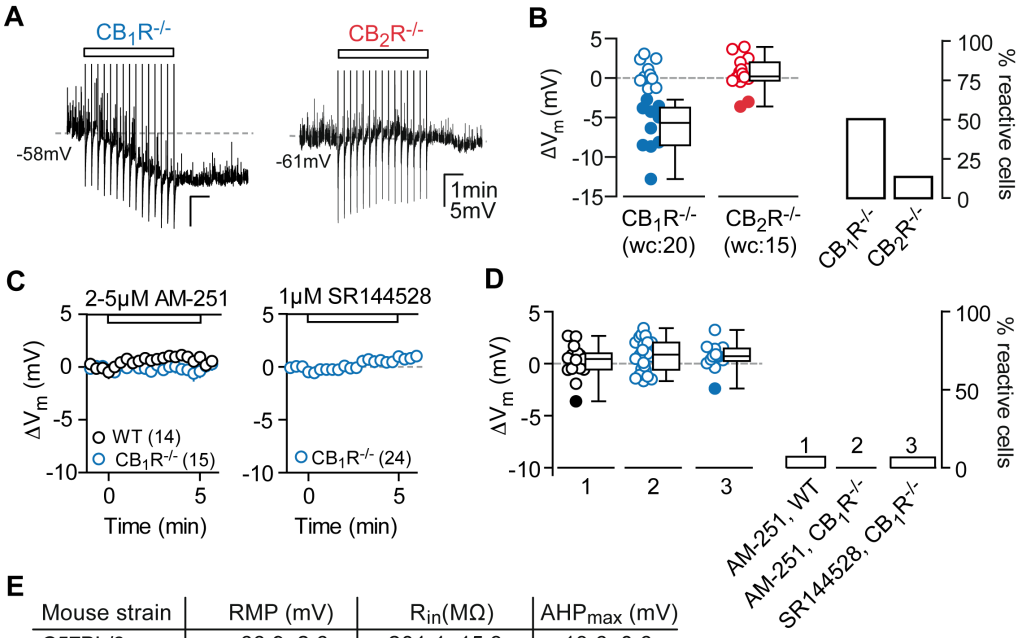

E

Mouse strain	RMP (mV)	R_{in}(MΩ)	AHP_{max} (mV)
C57BL/6	-66.9±2.6	201.1±15.8	-13.6±0.6
DAGLα KO	-65.5±1.9	260.1±26.9	-12.4±0.6
CB_1 R KO	-68.6±1.9	233.3±25.9	-13.3±1.3
CB_2R KO	-70.9±3	226.6±28.4	-12.8±1.9
Syn-CB_2 KO	-67.5±1.7	210.6±38.1	-10.8±1.1
	ns	ns	ns

Figure S3. Related to Figure 3. Cannabinoid receptor antagonists abolish the hyperpolarisation. (**A**) Whole-cell current-clamp recordings from both CB_1R and CB_2R KO animal lines confirm the results obtained in pp configuration as shown by the exemplary V_m traces of a $CB_1R^{-/-}$ (left) and $CB_2R^{-/-}$ CA3 PCs (right) recorded in wc configuration. (**B**) Left: summary box plot of the median ΔV_m (with 25th and 75th percentile) for reactive $CB_1R^{-/-}$ CA3 PCs (n(N)=20(5): -5.6, -8.5 and -3.7mV) and all $CB_2R^{-/-}$ CA3 PCs (n(N)=15(3): 0.21, -0.31 and 2mV). The V_m of $CB_2R^{-/-}$ CA3 PCs after the induction protocol did not differ significantly from baseline, whereas it did differ significantly for $CB_1R^{-/-}$ (paired t-test: P=0.45 and P=0.007 respectively). Right: the percentage of reactive cells for all recorded $CB_1R^{-/-}$ and $CB_2R^{-/-}$ CA3 PCs (50% vs. 13.3%). (**C**) Summary time course of the average ΔV_m in response to the action potential stimulus of whole-cell CA3 PCs recordings in slices of WT (n(N)=14(3)) and CB_1R KO mice (n(N)=15(3)) preincubated in the CBR antagonist 2-5μM AM-251 (left) and slices of CB_1R KO mice preincubated in the CB_2R-specific antagonist 1μM SR (right, n(N)=24(3)). (**D**) Left: the ΔV_m of each recorded cell (circles) and the median, 25thand 75th percentile of the average ΔV_m are shown for WT in AM-251 (0.72, 0.27 and 1.5mV), CB_1R KO in AM-251 (0.45, -0.56 and 1mV) and CB_1R KO in SR (0.88, -0.58 and 2.05mV). Right: the percentage of reactive CA3 PCs is shown for WT in AM-251 (7.1%), $CB_1R^{-/-}$ in AM-251 (0%) and $CB_1R^{-/-}$ in SR (6.7%). Filled circles indicate reactive cells. (**E**) Comparison of intrinsic electrophysiological parameters of CA3 PCs recorded in pp configuration revealed no significant differences between C57BL/6 WT and the different KO mouse strains.

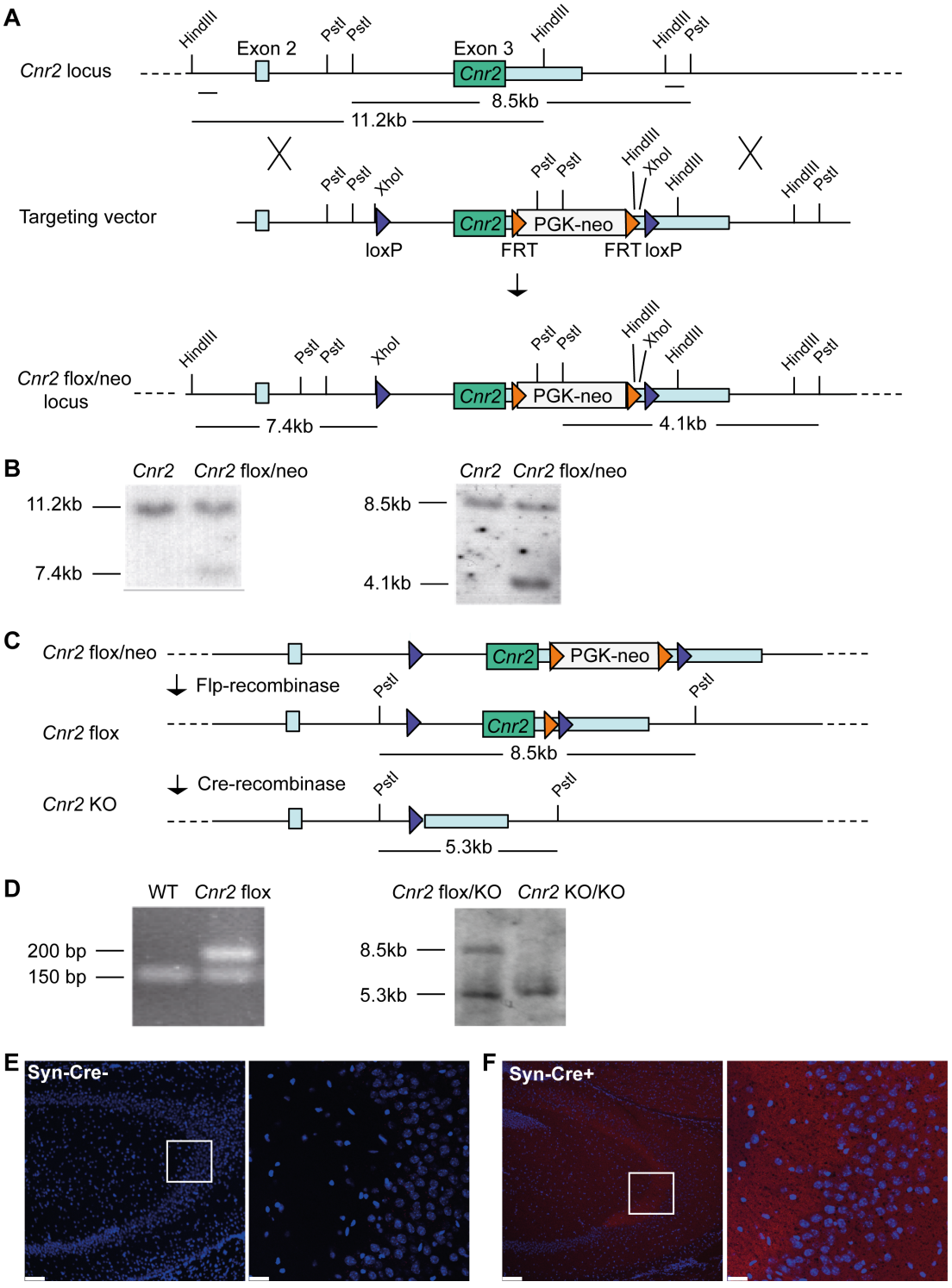

Figure S4. Related to Figure 3. Conditional Cnr2 targeting strategy. (**A**) *Cnr2* exons 2 and 3 are indicated as boxes, with the *Cnr2* coding region in dark green. The targeting vector contained a PGK-neo selection cassette, flanked by two FRT sites, in the 3' UTR. LoxP sequences were inserted in the intron between exons 2 and 3, as well as downstream of the PGK-neo cassette. (**B**) Recombinant ES cell clones were identified by Southern blotting with flanking 3' and 5' probes. (**C**) Mice carrying the *Cnr2* flox/neo locus were first crossed with a Flp-deleter mouse

strain, resulting in offspring with a *Cnr2* flox locus. (**D**) These animals are routinely genotyped by a PCR strategy. (**E-F**) Confocal images of the hippocampus of Syn-Cre- (E) and Rosa26-Stop-tdTomato-Syn-Cre+ reporter mice (F). Left panels: Overview of the hippocampus (scale bar: 100µm), right panels: higher magnification (scale bar: 25 µm) of area CA3. The confocal images clearly show the Syn-Cre expression in the hippocampus.

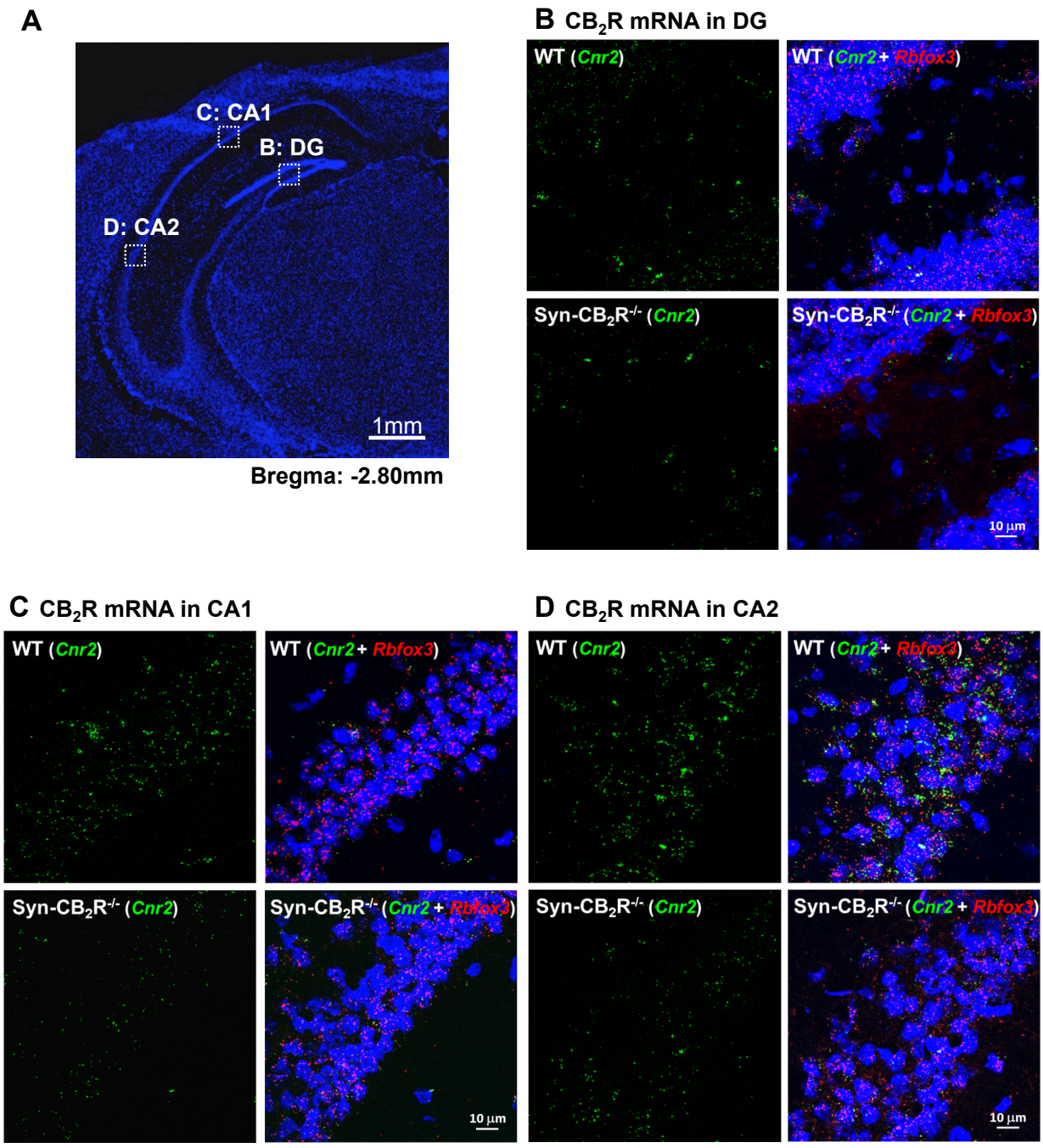

Figure S5. Related to Figure 4. CB_2R mRNA expression in the DG, CA1 and CA2 regions of the hippocampus as detected by RNAscope ISH. (**A**) Hippocampal image (DAPI staining), illustrating the target regions. (**B-D**) CB_2R mRNA (*Cnr2*, green) staining and co-localisation of CB_2R and NeuN (*Rbfox3*, red) mRNA in the DG (B), CA1 (C) and CA2 (D) of the hippocampus in WT (upper panels) and Syn-$CB_2R^{-/-}$ (lower panels) mice, illustrating a substantial reduction in CB_2R mRNA expression in Syn-CB_2R KO compared to WT mice. Note that the overall density of CB_2R mRNA in the DG and area CA1 is much lower than that in area CA2 or CA3 (see Figure 4).

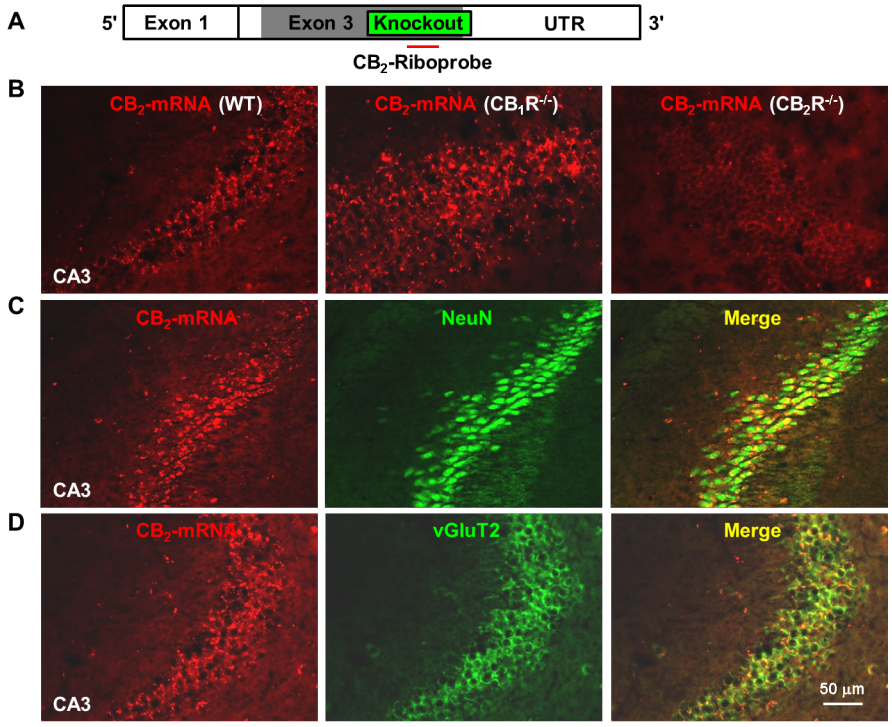

Figure S6. Related to Figure 4. CB_2R mRNA expression in area CA3 of mouse hippocampus by classical *ISH* assay. (**A**) The CB_2R mRNA structure in const. $CB_2R^{-/-}$ mice and the target region of a CB_2R probe used to detect CB_2R mRNA in the hippocampus of WT, $CB_1R^{-/-}$ and $CB_2R^{-/-}$ mice. This CB_2R-riboprobe targets the deleted region of the *Cnr2* gene in $CB_2R^{-/-}$ mice. (**B**) The CB_2R-riboprobe detected CB_2R mRNA in the CA3 region of hippocampus in WT and $CB_1R^{-/-}$, but not in $CB_2R^{-/-}$ mice. (**C-D**) Double-label fluorescent images, illustrating CB_2R mRNA (by ISH, red) is co-localised with NeuN (immunostaining, green) in hippocampal neurons (C) and also with vGluT2 (immunostaining, green) in hippocampal glutamatergic neurons (D) in WT mice.

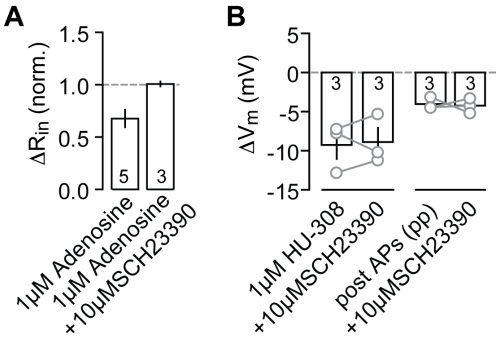

Figure S7. Related to Figure 5. Control of conductance-based R_{in} change mediated by adenosine-dependent activation of GIRK. (**A**) As a control, the relative change in R_{in} in response to 1µM Adenosine (n(N)=5(2): 0.67±0.08) is shown that was reversed by the application of the GIRK blocker 10µM SCH-23390 (1.01±0.02). (**B**) Acute application of SCH-23390 does not reverse the agonist- or AP-induced hyperpolarisation and thus excludes the involvement of GIRK channels. Left: single experiments (grey circles) and mean±SEM of n(N)=3(2) wc recordings showing the ΔV_m in HU and after SCH-23390 application (-9.3±1.8 and -8.9±1.8mV, paired t-test: P=0.82). Right: single experiments (grey circles) and mean±SEM of n(N)=3(2) pp recordings showing the ΔV_m after AP induction and with subsequent SCH-23390 application (-4±0.4 and -4.2±0.5mV, paired t-test: P=0.83).

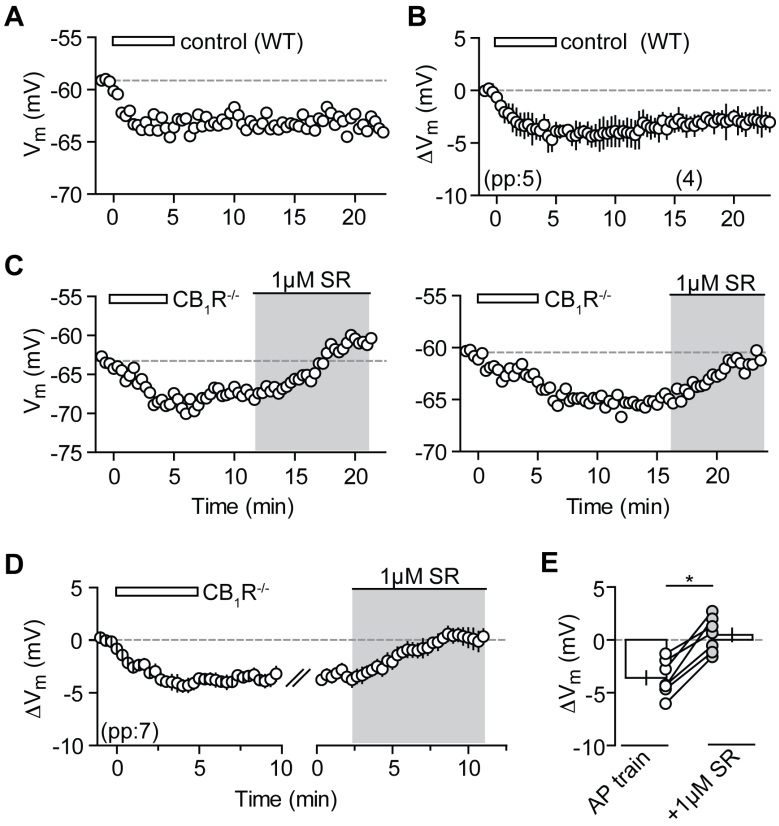

Figure S8. Related to Figure 6. Washin of the CB_2R inverse agonist SR acutely reverses the AP-induced hyperpolarisation. PP recordings of CA3 PCs in CB_1R KO and WT mice show that the V_m hyperpolarisation can be reversed by washin of 1µM SR. (**A**) Exemplary time plot of the V_m of a WT CA3 PC that was recorded for >15min post induction (AP train: rectangle). (**B**) Summary time plot of the average ΔV_m from n(N)=5(5) control WT CA3 PCs. At min15-20 the ΔV_m is still significantly different from baseline (-3.07±0.29mV; paired t-test: $p<0.05$). Note that this data is also included in Fig. 1. (**C**) Exemplary recordings of CB_1R-lacking CA3 PCs in which SR (grey) was washed in at different time points after the induction. (**D**) Summary time plot of n(N)=7(6) experiments in CB_1R KOs. (**E**) Before-after plot of each experiment showing the maximal ΔV_m after the AP train and the average ΔV_m of 10-15min after wash-in of SR. The mean average ΔV_m after the AP train (-3.6±0.63mV) after the AP train is significantly different from the mean ΔV_m after SR application (0.48±0.62mV; Wilcoxon matched pairs test: P=0.016). Furthermore, the V_m in SR does not differ from baseline values (Wilcoxon test: P=0.47).

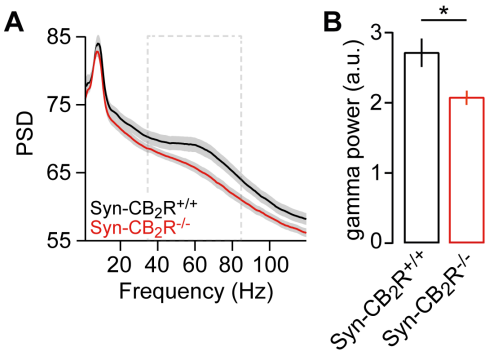

Figure S9. Related to Figure 8. Reduced power of gamma oscillations in area CA3 in Syn-$CB_2R^{-/-}$ mice. Average LFP power spectra (**A**) and cumulative power (**B**) in the 30-85Hz frequency band (grey rectangle in (A)) of control Syn-$CB_2R^{+/+}$ (n(N)=13(4)) and Syn-$CB_2R^{-/-}$ mice (n(N)=16(5), $F_{1,20}$=6.8, P=0.02). Data are presented as mean± SEM.

Supplemental Methods

Ethics statement and animal handling.

Animal husbandry and experimental procedures were performed in accordance with the guidelines of local authorities (Berlin, Germany), the German Animal Welfare Act and the European Council Directive 86/609/EEC. Animals were housed on a 12:12h day-night cycle with food and water available ad libitum. Constitutive CB_1R-, CB_2R-, and DAGLα KO mice (Buckley et al., 2000; Jenniches et al., 2015; Zimmer et al., 1999) were bred using a homozygous breeding protocol. Additionally, a subset of constitutive CB_2R KO mice was bred from heterozygous parents and their WT littermates were used as controls. Neuron-specific, conditional KO mice for CB_2R were generated using the Cre/loxP technology. To this purpose, transgenic mice expressing Cre recombinase under the Synapsin I promoter were bred with floxed CB_2R animals (see below). In this case, Cre-negative offspring was used as a control. DNA isolation and genotyping were performed according to standard protocols. All KO mice were maintained on a C57BL/6J genetic background.

Generation of conditional CNR2 knockout mice.

Two loxP sites were inserted into the Cnr2 gene flanking the coding exon 2 by homologous recombination into embryonic stem cells. An FRT-flanked neo selection cassette was also inserted upstream of the loxP site in the 3' untranslated region. Recombinant ES cell clones were identified by Southern blotting with flanking 5' and 3' probes. One clone was used for the generation of chimeric animals. Mice with the recombinant Cnr2-flox/neo locus derived from these chimeras were mated with a Flp-deleter strain in order to remove the PGK-neo selection cassette, resulting in a floxed Cnr2 locus (see Figure S3). To control for the specific expression of Cre under the Synapsin promoter, Syn-Cre mice were bred with the Rosa-26-Stop-tdTomato reporter line. Rosa-CAG-LSL-tdTomato-WPRE:deltaNeo has a loxP-flanked STOP cassette preventing transcription of the downstream red fluorescent protein variant (tdTomato). When bred to mice that express Cre recombinase, the resulting offspring will have the STOP cassette deleted in the cre-expressing tissue(s) resulting in expression of tdTomato (Madisen et al., 2010). The brains of the offspring were removed, snap-frozen in isopentane on dry ice and stored at -80°C until use. Brains were then embedded in Tissue-Tek® and consecutively sectioned at 16µm using a Leica cryostat and stored at -20°C until use. The sections were covered with Fluromont and images were acquired on a Zeiss Axioplan confocal microscope.

In vitro electrophysiology.

Slice preparation. Hippocampal slices were prepared from P21-P35 C57BL/6 and KO mice, and Wistar rats (where indicated). Animals were anesthetised with isoflurane and decapitated. Their brains were quickly removed and transferred to sucrose-based ice-cold artificial cerebrospinal fluid (aCSF) containing (in mM): 87 NaCl, 26 $NaHCO_3$, 50 Sucrose, 10 Glucose, 2.5 KCl, 1.25 NaH_2PO_4, 3 $MgCl_2$, 0.5 $CaCl_2$ for mice and 87 NaCl, 26 $NaHCO_3$, 75 Sucrose, 25 Glucose, 2.5 KCl, 1.25 NaH_2PO_4, 3 $MgCl_2$, 0.5 $CaCl_2$ for rats, respectively. Tissue blocks containing the hippocampus were mounted on a VT1200SVibratome (Leica, Germany) and horizontal slices of 300µm thickness were cut. Slices were subsequently stored for 1-5h in an interface chamber (Haas et al., 1979) at near-physiological temperature (~35°C) and superfused with aCSF containing (in mM): 119 NaCl, 26 $NaHCO_3$, 10 Glucose, 2.5 KCl, 1 NaH_2PO_4, 1.3 $MgCl_2$, 2.5 $CaCl_2$ (pH 7.4; 285-300mOsm; ~1ml/ min). All aCSF was equilibrated with 95% O_2 and 5% CO_2.

General setup. Individual hippocampal slices were transferred to a submerged chamber (Luigs and Neumann, Germany), perfused with aCSF (~5ml/ min, heated to 33-34°C) and visualised with infrared differential interference contrast optics on an Olympus BX-51 WI microscope. Extracellular field and patch-clamp recordings were performed with a MultiClamp 700A amplifier (Axon Instruments, USA) and monitored using an HM1507-3 oscilloscope (Hameg, Germany). Signals were filtered at 2-4 kHz, digitised at 5-10 kHz with 16-bit resolution using a BNC-2090 interface board (PCI 6035E A/D Board, National Instruments, USA) and recorded in IGOR Pro 5.0 (WaveMetrics Inc., USA) with custom-made plug-ins. Putative hippocampal principal cells were identified based on their location, morphology and electrophysiological properties. CA2 PCs were additionally filled with 30µM Alexa and post-hoc identified under a fluorescence microscope (Leica DMI4000 B, Germany) according to their dendritic arborisation. They can be distinguished from neighbouring CA3a PCs by their characteristic dendritic bifurcation close to the soma (Wittner and Miles, 2007).

Pharmacological agents. All drugs were purchased from Tocris (Germany) or Cayman Chemical (via Biomol, Germany). If not stated otherwise, experiments were performed in the continuous presence of $GABA_A$- and $GABA_BR$ blockers (1µM gabazine and CGP55845 respectively) to isolate excitatory transmission, and 100nM NBQX to prevent epileptiform activity. For recording $GABA_AR$-mediated eIPSCs, the aCSF was supplemented with 25µM D-AP5, 10µM NBQX and 1µM CGP55845 to block AMPAR-, NMDAR- and $GABA_BR$-mediated transmission respectively. Field recordings were performed in aCSF only. Additional drugs were bath applied to the whole slice. CBR (inverse) agonists used were the following: AM-251 (2-5µM), SR (1µM), 2-AG (10µM), WIN 55,212-2 (1µM) and HU-308 (1µM).

Whole-cell and perforated patch recordings. Patch pipettes were pulled from borosilicate filamented glass capillaries (Harvard Apparatus, UK; 1.5 mm OD) with a DMZ Universal Puller (Zeiss, Germany) and fire-polished to a final resistance of 2-3 MΩ for wc recordings. Pipettes were backfilled with filtered internal solution containing (in mM): 130 $KMeSO_3$ (or, in some experiments, 140 $KMeSO_4$), 10 KCl, 10 HEPES, 4 NaCl, 4 Mg-ATP, 0.5 Na-GTP, 5 phosphocreatine, 285–290 mOsm, pH was adjusted to 7.3 with KOH. For pp recordings, pipettes with a final resistance of 3-4 MΩ were tip-filled with the same internal solution. They were then backfilled with internal solution additionally supplemented with gramicidin (80µg/ml) which was prepared as a stock solution (20mg/ ml, diluted in DMSO) on the day of use. For experiments with intracellular application of the non-hydrolysable GDP analogue GDP-β-S, Na-GTP in the internal solution was replaced with GDP-β-S, which was added freshly on the day of use.

All recordings, unless indicated differently, were performed in current-clamp mode. The resting V_m and input resistance (R_{in}) were determined directly after establishing the wc configuration or, for pp recordings, when the access resistance (R_a) had stabilised. Experiments were only continued if cells had a resting V_m more hyperpolarised than -55mV (not corrected for liquid junction potential, LJP). The cells were further characterised by recording their membrane response / firing pattern to current injections of increasing strengths (-20 to +800pA, increment: 20-50pA, 1s). Afterwards, the V_m was adjusted to -60mV with continuous current injection if not stated otherwise. R_{in}, R_a and pipette capacitance were monitored continuously throughout the experiment and the latter two were compensated for using bridge balance and capacitance neutralisation. For pp recordings, only cells with a stable R_a below 60MΩ were used, with the exception of the dual pp experiments, where the control cell was used if a R_a below 100MΩ was achieved. Experiments were stopped if cells depolarised by more than 5mV or the R_a changed > 10% over the course of the recording.

Action potential protocols. The standard AP protocol used consisted of 15 trains with 50 APs each (750 APs, inter-stimulus interval: 10ms, inter-train interval: 20s). Individual APs were elicited by 2ms long, somatic current injections (1-2nA). The theta-burst protocol used to test the induction threshold of CA1 PCs consisted of 10 bursts of five stimuli (applied at 100Hz) with a 200ms inter-burst interval, repeated every 5s 60x (3000 APs). For the construction of the physiological spike train (PST), the unit activity of a putative CA3 place cell recorded in a rat

traversing a linear track rat was used (Diba and Buzsáki, 2008; Schmidt et al., 2009). More specifically, an AP protocol was implemented using a 5min stretch of inter-spike intervals of this cell's place field firing pattern. Because the PST stemmed from rat data, this dataset was acquired in rat accordingly.

Recordings of IPSCs. Pharmacologically isolated (25µM AP5 and 10µM NBQX), evoked IPSCs (denoted as eIPSCs in figures) were recorded in voltage-clamp configuration at a holding potential of -50 or -70mV (resulting in either out- or inward currents). The stimulation electrode (borosilicate glass, as above) was positioned in stratum radiatum of CA3 ~150µm away from the recorded cell (towards the hilar region of the dentate gyrus) and the experiment were only started when the evoked IPSCs displayed monosynaptic rise and decay kinetics. DSI was elicited by depolarising the cell to 0mV (3x 1s, 5s interval or 1x 5s). Cells that showed a >15% reduction in the amplitude of the evoked IPSCs after the depolarising step were considered DSI-positive. Pharmacologically isolated (25µM AP5 and 10µM NBQX), spontaneous IPSCs for the analysis of DSI were recorded with an internal solution containing 140mM KCl to reverse and increase the driving force for chloride and in the presence of 20µM carbachol to boost their frequency.

Recordings of synaptically evoked EPSPs and action potentials. To test for the change in spike probability of CA3 PCs before and after pharmacological CB_2R activation, a stimulation electrode was placed in stratum radiatum of CA3 and synaptic, glutamatergic responses (EPSPs) were evoked and recorded in current clamp in the continuous block of GABAergic transmission. The stimulation strength was adjusted to an initial spike probability of ~80%.

Extracellular field recordings. For field recordings, both the stimulation and recording pipette (borosilicate glass, as above; tip diameter: ~20µm) were filled with aCSF and placed in stratum radiatum of area CA3. Field EPSPs were evoked by stimulating presumptive associational/commissural fibres (duration: 100µs, frequency: 0.05Hz) using a stimulus isolator (Isoflex, A.M.P.I) and adjusted to 60% of the maximal amplitude. The fEPSP slopes were determined as dV/dt (in mV/ms) of 10 to 90% of the amplitude in each individual trace.

Data analysis. Data analysis was performed in IGOR Pro 6.12 using the IGOR analysis software package Neuromatic (www.neuromatic.thinkrandom.com). Statistical comparisons between groups were performed in GraphPad Prism (GraphPad Software, USA). Sample sizes are given as the number of experiments (n) and the number of animals (N). Individual membrane potential values (denoted as V_m in figures) were determined from a 10ms average around the detected minimum within a 100ms time window every 20s. The minimum average was taken to circumvent distortions due to the high spontaneous activity in CA3 PCs. V_m values are not corrected for LJP, which was calculated to be 10mV (JPCalcW, Molecular Devices; USA) (Barry, 1994) for the $KMeSO_3$-based internal solution. The R_{in} was calculated from a 50ms average of the steady-state V_m response to a hyperpolarising test pulse (400ms, -20 to -80pA). Given V_m values were normalised to a 1min baseline (3 values) before the AP induction protocol or, for drug application, to a 2min baseline. For summary time plots of the global V_m average, the individual values of all experiments were averaged per point in time; alternatively, the median (including 25^{th} and 75^{th} percentile) at a certain time point is calculated as the average of 1min (3 values/ experiment). For the analysis of spontaneous IPSCs (denoted as sIPSCs in figures), individual events were detected with a threshold-based algorithm in Neuromatic and a total of 5-10s were analysed for each time point. The amplitude of each event was defined as the 10ms average maximum within a 100ms time window after the stimulation. Examples show individual traces.

The distribution of data was assessed with the D'Agostino and Pearson omnibus normality test. Normally distributed data sets were compared with a two-tailed Student's t-test and values are expressed as mean±SEM. Nonparametric tests were used as indicated and data presented as median (including the 25^{th} and 75^{th} percentile). The averages of the change in membrane potential (ΔV_m) across cells were assessed with the appropriate paired tests (Student's t-test or, if indicated, Wilcoxon signed-rank test). Correlation analyses were carried out using either the Pearson (for data sampled from Gaussian distribution, indicated by r) or Spearman (nonparametric, indicated by r_s) correlation coefficient. Results were considered significant at $p<0.05$. The percentage of reactive cells in each experiment was calculated from a -2.1mV cut-off to facilitate the comparison between different (recording-)

conditions/manipulations. This cut-off was based on the mean of the wc hyperpolarisation (-1.8mV) plus its standard error (-0.3mV). To give a 'biologically relevant' estimate of the average ΔV_m, only the values of reactive cells are averaged for data sets in which washout in the wc configuration led to a skewed data distribution.

The electrophysiological analysis of the const. (1) and cre-dependent (2) CB_2R KO animals, were partially (1) and fully (2) performed in a blind and interleaved manner. In case of the const. CB_2R KOs, the results of cells from heterozygously bred WT and KO littermates, that were recorded and analysed blind, were not different from homozygously bred KO and C57BL/6 WT mice (Mann-Whitney test: P=0.8) and the data was thus pooled.

In vivo electrophysiology.

Wire array recordings. After one week of handling and habituation to the recording room, mice were implanted under isoflurane anesthesia with arrays of single tungsten wires (40µm, California Fine Wire Company) in the CA3 area (coordinates relative to bregma, anteroposterior: -1.94mm, lateral: 2.3mm, ventral: 2.15mm). Reference and ground electrodes were miniature stainless-steel screws in the skull above the cerebellum. Implanted electrodes were secured on the skull with dental acrylic. After one week of recovery, animals were placed in a 1x1m open arena and were allowed to explore freely during recordings. Electrodes were connected to operational amplifiers (Neuralynx, USA) to eliminate cable movement artefacts. Electrophysiological signals were differentially amplified, bandpass filtered (1-9000Hz) and acquired continuously at 30303Hz. After 1h of baseline recordings animals were injected with either vehicle (10mg/kg DMSO) or with HU-308 (10mg/kg, dissolved in DMSO) and were recorded in the arena for one more hour. After completion of the experiments, mice were deeply anesthetised and electrolytic lesions at selected recording sites were performed. Subsequently the animals were perfused intracardially with 4% PFA solution and decapitated. Brains were fixed, cut into 50µm slices and stained with cresyl violet for confirmation of recording sites.

Data analysis. Signal processing was carried out off-line by custom-written MATLAB algorithms. The LFP was processed by low-pass filtering and down-sampling of the wideband signal to 1250Hz. Phase-amplitude coupling of theta and gamma oscillations was assessed for epochs of theta oscillations with a theta/delta power ratio of at least five. The theta phase was obtained by Hilbert transformation of the 5-10Hz filtered signal. Gamma oscillation peaks were detected in the 30-85Hz and 65-120Hz band-pass filtered signal, and their amplitudes and theta phases were subsequently calculated. The gamma amplitude – theta phase modulation coefficient was computed as a correlation coefficient (Fisher z-transformed, Pearson's or Spearman's, depending on the distribution normality) between the gamma modulation depth (Wulff et al., 2009) and the theta/delta ratio-standardised amplitude of the concurrent theta oscillation. Power spectral density was computed using the multitaper method (NW 3, window size 1024) and standardised to the power in the 30-45Hz band during baseline recordings. The statistical significance of comparisons was determined by a two-way ANOVA (subject x treatment and subject x genotype).

In situ hybridisation and immunohistochemistry

Classical In situ hybridisation. Animals (WT, $CB_1R^{-/-}$, and $CB_2R^{-/-}$; 2 mice each strain) used in this experiment were matched for age (6-8weeks) and weight (20–30g). The const. $CB_2R^{-/-}$ mice are C terminal-deleted, in which the last 341bp on exon 3 are deleted that encode parts of the intracellular and extracellular third loops, transmembrane regions 6 and 7, and the intracellular C terminus (Buckley et al., 2000; Zhang et al., 2014). These animals were deeply anesthetised and transcardially perfused with saline, followed by 4% Paraformaldehyde (PFA). CB_2R-mRNA riboprobe was synthesised as described in our previous report (Zhang et al., 2014). The ISH procedures for hippocampal CB_2R mRNA expression were the same as reported previously (Lanciego et al., 2011; Zhang et al., 2014). To determine the phenotype of mCB_2R mRNA-expressing neurons in hippocampus, we used

fluorescent IHC to label all neurons with a NeuN antibody or glutamatergic neurons with a vGlut2 antibody, respectively. After the mCB_2R mRNA staining in freely floating coronal slices by classical ISH, the sections were incubated with a mouse anti-NeuN antibody (1:1,000; Millipore) or a mouse anti-vGlut2 antibody (1:500; Millipore) at 4°C overnight, followed by Alexa Fluor 488 goat anti-mouse IgG (1:500; Molecular Probes) at RT for 2h. The sections were mounted on glass slides, air-dried at RT, and coverslipped with Fluorogel and Tris buffer (Electron Microscopy Sciences).

RNAscope In situ hybridisation. Animals (WT, Syn- $CB_2R^{-/-}$, and $CB_2R^{-/-}$ mice; 2-3 mice each strain, age 4-8 weeks) were perfused with saline to wash out blood cells in the brains, and then quickly decapitated. The whole brains were taken out, quickly frozen on dry ice, and then stored at -80°C for CB_2R RNAscope ISH assays. The brains were sectioned coronally (14μm thick, -2.8mm posterior to bregma) to sample the hippocampus (Paxinos and Watson, 2005). The freshly frozen sections were then mounted on positively charged microscopic glass slides (Fisher Scientific). A CB_2R-specific probe (Mm-*Cnr2*-O2) that targets the *Cnr2* gene-deleted region on exon 3 (506-934bp of NM_009924.4) and a NeuN probe (Mm-*Rbfox3*-C2) that targets 1827-3068bp of NM_001039167.1 were designed and provided by Advanced Cell Diagnostics Inc. The CB_2R/NeuN mRNA staining was performed following the User Manual for Freshly Frozen Tissue using the RNAscope Multiplex Fluorescent Reagent Kit (Advanced Cell Diagnostics). Stained slides were coverslipped with fluorescent mounting medium (ProLong Gold Antifade Reagent P36930, Life Technologies) and scanned into digital images with an Olympus FluoView FV1000 confocal microscope at 60× magnification using manufacturer-provided software.

Fluorescence-activated cell sorting (FACS). The frozen, -80°C cold whole brains were then put into a -20°C cryostat to equilibrate for at least 30min before dissection. The dissection procedure was the same as reported previously (Li et al., 2015; Liu et al., 2014; Rubio et al., 2015) with very minor modifications. Briefly, 1.5mm thick coronal hippocampal sections were cut at the levels of bregma - 2.27 and - 3.77mm, and then hippocampal tissues were punched with a 24gauge neuron punch needle (Fine Science Tools). After finely mincing the hippocampal tissue with razor blades on ice, it was transferred into 1ml of ice-cold Hibernate A (HA-if, Brain Bits). After centrifuging at 3,000rpm (4°C) for about 2min, the supernatant was discarded and the pellets were re-suspended in 0.6ml of ice-cold Hibernate A. Each sample was first triturated 10x in series using fire-polished glass pipettes (with successively smaller diameters of 1.0mm and 0.4mm), and then the samples were triturated for additional two times with 0.4mm-diameter glass pipettes. Each trituration step consisted of triturating up and down at least 1x. After centrifuging for 5min at 3,500rpm (4°C), the collected cells were re-suspended with 0.5ml of ice-cold Hibernate A. The cell pellets were then fixed and permeabilised by adding the same volume of 100% of cold ethanol (-20°C) for 15min on ice. After centrifuging for 4min at 4,000rpm (4°C), the cell pellets were re-suspended with 0.5ml PBS and incubated with a PE-labeled (fluorescent) anti-NeuN antibody (1:500; FCMAB317PE, Millipore) at 4°C for 30min. Then the cells were washed 3x with 0.5-1.0ml cold PBS. After the cells were filtered with 40μm cell strainers (Falcon brand; BD Biosciences), NeuN-positive and NeuN-negative cells were sorted by a FACSAria I cell sorting system (BD Biosciences). The sorted neurons or cells can be identified by the distinct forward (FSC) and side (SSC) scatter properties. DAPI (1 μg/ml, staining DNA) staining indicated that 98% of the events in the neuronal gate are DAPI-positive events (nucleated cells). After defining the cell population, we gated single cells by FCS width and height, in which ~98% of single cells were DAPI positive. This single-cell population was sorted again to separate NeuN-positive hippocampal neurons (with PE fluorescent signal) and NeuN-negative non-neuronal cells (not PE fluorescent) (approximately 5000 cells for each group) for the following CB_2R mRNA qPCR assays. The sorted cells were collected into 1.5ml Eppendorf tube containing 50μl extraction buffers (PicoPure RNA isolation kit, Arcturus Bioscience) and then suspended by pipetting up and down 10x, followed by incubation at 42°C for 30min. After centrifuging the suspension at 3,500 at 4°C for 2min, the supernatant were collected for the RNA extraction according to the manufacturer's protocol for using PicoPure RNA isolation kit (Arcturus Bioscience) to extract RNA. After the RNA extraction, the cDNA was synthesised by use of Superscript III first strand cDNA synthesis kit (Invitrogen). We used gene-targeted preamplification of cDNA as described previously (Li et al., 2015; Liu et al., 2014; Rubio et al., 2015). First, we pooled TaqMan ABI primer/probes (20×TaqMan gene expression assay as a

stock solution) for all the target genes listed in Table 1. Each cDNA sample (10µl) was mixed with the pooled primer solution (10µl) and 20µl of 2×TaqMan PreAmp Master Mix (Applied Biosystems). The cDNA preamplification was performed in a Veriti 96-well Thermal Cycler (Applied Biosystem) using the following program: 95°C hold for 10min, denaturation at 95°C for 15s, and annealing and extension at 60°C for 4min (14 cycles). The preamplified cDNA product was diluted 10x before proceeding for qPCR assays. The qPCR was performed in duplicates with a FAM-labeled probe for each target gene and a VIC-labeled probe for an endogenous control gene (*Gapdh*). We used TaqMan Advanced Fast PCR Master Mix (7500 Fast TaqMan instrument, Life Technologies) for qPCR, using the following program: 95°C hold for 20s, then 40 cycles with denaturation at 95°C for 3s, and annealing and extension at 60°C for 30s. The ΔΔCt method with *Gapdh* as the housekeeping gene was used to analyse the PCR reactions. The uniformity of the preamplification was verified by comparing cDNA templates with the unamplified and preamplified samples (data not shown).

Table 1. **Related to experimental procedures.** Gene expression assays and primer or probe sequences for FACS

Gene **(Protein)**	**TaqMan probe[a] or Assay ID[b]/Cat. no[c]**	**Forward primer**	**Reverse primer**
Cnr2 (CB_2R)	ATGCTGGTTCCCTGCAC[a]	AGCTCGGATGCGGCTAGAC	AGGCTGTGGCCCATGAGA
Cnr1 (CB_1R)	Mm01212171_s1[b]		
Rbfox3 (NeuN)	Mm01248771_m1[b]		
Itgam (CD11b)	Mm00434455_m1[b]		
Cspg4 (NG-2)	Mm00507257_m1[b]		
Aldh1l1 (ALDH1L1)	Mm03048957_m1[b]		
Gapdh (GAPDH)	4352339E[c]		

Statistics analysis. Data is presented as mean ± S.E.M. One-way ANOVA was used to analyse the difference between WT and 2 CB_2R-KO mice in terms of different target gene expression in NeuN-positive and NeuN-negative cells. Individual group comparisons were carried out using the Student–Newman–Keuls method.

Supplemental references

Barry, P.H. (1994). JPCalc, a software package for calculating liquid junction potential corrections in patch-clamp, intracellular, epithelial and bilayer measurements and for correcting junction potential measurements. J. Neurosci. Methods *51*, 107–116.

Diba, K., and Buzsáki, G. (2008). Hippocampal network dynamics constrain the time lag between pyramidal cells across modified environments. J. Neurosci. *28*, 13448–13456.

Haas, H.L., Schaerer, B., and Vosmansky, M. (1979). A simple perfusion chamber for the study of nervous tissue slices in vitro. J. Neurosci. Methods *1*, 323–325.

Lanciego, J.L., Barroso-Chinea, P., Rico, A.J., Conte-Perales, L., Callén, L., Roda, E., Gómez-Bautista, V., López, I.P., Lluis, C., Labandeira-García, J.L., et al. (2011). Expression of the mRNA coding the cannabinoid receptor 2 in the pallidal complex of Macaca fascicularis. J. Psychopharmacol. *25*, 97–104.

Madisen, L., Zwingman, T.A., Sunkin, S.M., Oh, S.W., Zariwa, a H., Gu, H., Ng, L.L., Palmiter, R.D., Hawrylycz, M.J., Jones, A., et al. (2010). A robust and high-throughput Cre reporting and characterization system for the whole mouse brain. Nat. Neurosci. 13, 133–140.

Paxinos, G., and Watson, C. (2005). The rat brain in stereotaxic coordinates. (Elsevier Academic Press).

Rubio, F.J., Liu, Q.-R., Li, X., Cruz, F.C., Leao, R.M., Warren, B.L., Kambhampati, S., Babin, K.R., McPherson, K.B., Cimbro, R., et al. (2015). Context-Induced Reinstatement of Methamphetamine Seeking Is Associated with Unique Molecular Alterations in Fos-Expressing Dorsolateral Striatum Neurons. J. Neurosci. *35*, 5625–5639.

Schmidt, R., Diba, K., Leibold, C., Schmitz, D., Buzsáki, G., and Kempter, R. (2009). Single-trial phase precession in the hippocampus. J. Neurosci. *29*, 13232–13241.